



HAL
open science

Comparative study of continuum damage mechanics and Mechanics of Porous Media based on multi-mechanism model on Polyamide 6 semi-crystalline polymer

M. Jeridi, Lucien Laiarinandrasana, Kacem Sai

► To cite this version:

M. Jeridi, Lucien Laiarinandrasana, Kacem Sai. Comparative study of continuum damage mechanics and Mechanics of Porous Media based on multi-mechanism model on Polyamide 6 semi-crystalline polymer. *International Journal of Solids and Structures*, 2015, 53, pp.12-27. 10.1016/j.ijsolstr.2014.10.031 . hal-01101447

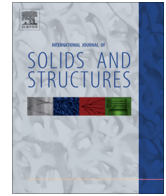
HAL Id: hal-01101447

<https://minesparis-psl.hal.science/hal-01101447>

Submitted on 3 Aug 2018

HAL is a multi-disciplinary open access archive for the deposit and dissemination of scientific research documents, whether they are published or not. The documents may come from teaching and research institutions in France or abroad, or from public or private research centers.

L'archive ouverte pluridisciplinaire **HAL**, est destinée au dépôt et à la diffusion de documents scientifiques de niveau recherche, publiés ou non, émanant des établissements d'enseignement et de recherche français ou étrangers, des laboratoires publics ou privés.



Comparative study of continuum damage mechanics and Mechanics of Porous Media based on multi-mechanism model on Polyamide 6 semi-crystalline polymer



M. Jeridi^a, L. Laiarinandrasana^b, K. Sai^{a,*}

^aUGPMM, Ecole Nationale d'Ingénieurs de Sfax, BP 1173 Sfax, Tunisia

^bMINES ParisTech, Centre des Matériaux, CNRS UMR 7633, BP 87, 91003 Evry Cedex, France

ARTICLE INFO

Article history:

Received 7 June 2014

Received in revised form 23 October 2014

Available online 6 November 2014

Keywords:

Semi-crystalline polymers

Gurson

Damage

Continuum damage mechanics

Multi-mechanism model

ABSTRACT

The biphasic character of semi-crystalline polymer was modeled by the multi-mechanism (MM) constitutive relationships. Here, a comparative study between continuum damage mechanics (CDM) theory and Mechanics of Porous Media (MPM) approach, both related to the MM model, is performed. This comparison is based upon creep tests conducted on notched round bars made of PA6 semi-crystalline polymer to enhance a multiaxial stress state. For CDM model, the damage is classically described by a unique overall variable whereas the average of the local porosity at each phase level was considered for the MPM model. For each model, the optimization of the set of material's parameters was carried out by combining the overall behavior of notched specimens subjected to creep loading, as well as the local information such as the distribution of porosity. It is found that both CDM and MPM models, each coupled with MM model correctly describe the overall creep behavior of the notched specimen if two damage variables are used. Moreover the MM/MPM model is more relevant for predicting porosity distribution.

© 2014 Elsevier Ltd. All rights reserved.

1. Introduction

The frequent use of polymers in engineering components requires reliable constitutive models to describe both their mechanical and damage behaviors. Among these materials, semi-crystalline polymers (SCP) exhibit high non linear mechanical response caused by their structural changes that necessitates the development of accurate constitutive models. These models should be based on deformation and damage mechanisms to analyze inelastic behaviors of structures made of SCP. During the two last decades, extensive research was accomplished on the investigation of the behavior of SCP materials. These works are of two kinds (i) constitutive models (ii) durability (damage mechanics and failure).

- Examples of studies devoted to analyze SCP stress–strain response includes the works of [Dusunceli and Colak \(2007\)](#), [Drozdov and Christiansen \(2008\)](#), [Baudet et al. \(2009\)](#), [Bles et al. \(2009\)](#), [Drozdov \(2010\)](#), [Epee et al. \(2011\)](#), [Ricard et al. \(2014\)](#).

The large deformation level, the strain rate effect, the influence of the crystallinity ratio are factors that influence the SCP behavior, see for instance [Danielsson et al. \(2002\)](#), [Drozdov \(2010\)](#), [Epee et al. \(2011\)](#), [Drozdov \(2013\)](#), [Abu Al-Rub et al. \(2014\)](#).

- In addition to the factors enumerated above, SCP might contain initial voids that grow and coalesce during deformation and should be considered. Therefore, SCP are assumed to be porous media containing micro-voids in the undeformed state considered as damage. They are at the origin of failure by their coalescence during mechanical loading ([Laiarinandrasana et al., 2010](#); [Boisot et al., 2011](#)). The durability of the SCP was in the focus of a second class of researches. The durability prediction requires a better understanding of the failure mode of structures made of SCP, see for instance [Cotterell et al. \(2007\)](#), [Wang et al. \(2010\)](#), [Detrez et al. \(2011\)](#), [Frontini et al. \(2012\)](#), [Leevers \(2012\)](#), [Ricard et al. \(2014\)](#), [Abu Al-Rub et al. \(2014\)](#).

Two broad approaches have emerged in the literature to predict failure of materials: continuum damage mechanics (CDM) theory and the Mechanics of Porous Media (MPM) concept. The first class of model is known to provide good predictions under shear tensile loading condition where typically low stress triaxialities are encountered. Whereas, according to [Brunig et al. \(2013\)](#), for

* Corresponding author.

E-mail address: kacemsai@yahoo.fr (K. Sai).

instance, porous plasticity model type is more appropriate at high stress triaxialities.

- CDM theory describes the effects of growth on macroscopic variables. This approach has been extensively applied to metallic materials (Lemaitre and Desmorat, 2001; Hambli, 2001; Lemaitre et al., 2000; Chaboche et al., 2006; Saanouni, 2008; Boudifa et al., 2009; Ayoub et al., 2011). In the CDM approach, damage is modeled at the macroscopic level by means of thermodynamic variable that leads to elastic moduli degradation and may also affect the plastic behavior. This approach can be extended in order to include volumetric plastic strains that play important roles in the ductile fracture under high triaxialities (Brunig et al., 2013).
- MPM models such as that of Gurson–Tvergaard–Needleman (GTN), initiated by Gurson (1977) are based on the assumption that damage occurs at microstructural level due to micro-void nucleation, growth and coalescence. Void growth is linked to the plastic strain and the stress triaxiality level. This approach was adopted for instance by Pardoen and Hutchinson (2000), Besson and Guillemer-Neel (2003), Monchiet et al. (2008), Sai et al. (2011), Oral et al. (2012), Ognedal et al. (2014). Improvements was proposed in order to take into account the effects of low triaxiality during shearing (Nahshon and Hutchinson, 2008; Nielsen and Tvergaard, 2009; Tvergaard and Nielsen, 2010). Some difficulties may also be encountered by the porous plasticity models that are not able to correctly predict the crack propagation path (Hambli, 2001). Another limitation of the model is that nucleation of the voids does not occur under compression (Nahshon and Xue, 2009).

Comparative studies between the GTN porous plasticity models and the CDM theories have been performed for instance by Hambli (2001), Mkaddem et al. (2004), Pirondi et al. (2006), Li et al. (2011), Malcher et al. (2012), Andrade et al. (2014).

The present work is a continuation of previous studies devoted to propose reliable constitutive models that consider both mechanical and damage behavior of Polyamide 6 (PA6) and Polyamide 11 (PA11) subjected to tensile and creep loadings. These models belong to two distinct approaches (i) the so-called multi-mechanism (MM) formalism (Regrain et al., 2009; Regrain et al., 2009; Sai et al., 2011; Cayzac et al., 2013) (ii) the unified approach (mono-mechanism) (Lairinandasana et al., 2010). The first category is more appropriate for SCP since it allows the distinction of the two phases by means of the crystallinity index. Therefore, it provides local information such as, plastic strains, stresses and damage in each phase. Only multi-mechanism model will be then considered in the sequel. The MM formalism that considers both mechanical and damage behavior of SCP was used to study the void growth, the creep and tensile behavior and the damage localization in notched specimens. An attempt is then made here to enroll the same MM model to GTN and CDM theory.

The novelties in this work are two folds:

- Coupling the CDM theory and the MM model: to the authors' best knowledge this association has never been proposed before;
- For the two MM-associated models, it is proposed to consider the damage (i) as an intrinsic local variable related to each specific phase, (ii) as a unique overall variable over both phases.

The paper is organized in the following manner: Constitutive equations of the proposed MM models are detailed in section 2. To assess their reliability, the two MM models are compared with experimental data base taken from the works of Regrain et al.

(2009), Cayzac et al. (2013) in Section 3. A selection strategy is developed with the aim to choose the more relevant model. A first selection of the models is performed by comparison to creep behavior of notched specimen in Section 3.1. The local responses of the remaining models are then analyzed in Section 3.2 to retain the more appropriate model(s). The local contribution of damage state at each phase level is critically commented in Section 3.3.

2. Modeling

Since SCP consist of amorphous and crystalline phases, MM approach is good candidate to describe the polymeric material as a composite material. Amorphous and crystalline phases are, respectively, mapped to a first mechanism referred to as 'a' and a second mechanism referred to as 'c'. The MM approach is intended here to describe the contribution of the amorphous phase and the crystalline phase to the inelastic behavior of SCP characterized by their crystallinity ratio z .

The use of a finite strain formulation through updated lagrangian formalism is needed to model large-strain deformation of polymer. The material behavior is based on Green–Naghdi transformation of the stress–strain problem into an “equivalent material referential”. This kind of formulation can be applied to materials with tensorial internal variables without modifying the local evolution rules (Ladeveze, 1999). The model is described by:

$$\underline{\underline{L}} = \dot{\underline{\underline{F}}} \underline{\underline{F}}^{-1} \quad \underline{\underline{D}} = \frac{1}{2} (\underline{\underline{L}} + \underline{\underline{L}}^T) \quad \underline{\underline{\Omega}} = \frac{1}{2} (\underline{\underline{L}} - \underline{\underline{L}}^T) \quad (1)$$

where $\underline{\underline{F}}$ is the deformation gradient, $\underline{\underline{L}}$ the rate of deformation, $\underline{\underline{D}}$ the stretch rate and $\underline{\underline{\Omega}}$ the rotation rate. The stretch rate tensor is transported into a local rotated referential following the expression:

$$\dot{\underline{\underline{e}}} = \underline{\underline{R}}^T \underline{\underline{D}} \underline{\underline{R}} \quad (2)$$

where the rotation tensor $\underline{\underline{R}}$ is determined by the polar decomposition of the deformation gradient $\underline{\underline{F}} = \underline{\underline{R}} \underline{\underline{U}}$. $\underline{\underline{R}}$ and $\underline{\underline{U}}$ describe respectively a pure rotation and a pure stretch tensor.

The integrated strain tensor is decomposed into both elastic and inelastic parts. Thanks to updated lagrangian formulation, constitutive relations can be expressed as in small strain hypothesis. Therefore, dealing with the elastic strain tensor is equivalent to a hypoelastic formulation in agreement with a Green–Naghdi stress rate. The stress measure is here the Cauchy stress $\underline{\underline{\sigma}}$ obtained by using the conjugate stress $\underline{\underline{S}}$ which results from the material behavior integration:

$$\underline{\underline{\sigma}} = \det^{-1}(\underline{\underline{F}}) \underline{\underline{R}} \underline{\underline{S}} \underline{\underline{R}}^T \quad (3)$$

Under the small deformation hypothesis and using the assumption of uniform elasticity, the total strain can be decomposed into an elastic part and an inelastic one.

$$\underline{\underline{\epsilon}} = \underline{\underline{\epsilon}}^e + \underline{\underline{\epsilon}}^{in} \quad (4)$$

The assumption of uniform strain in the semi-crystalline polymers was also made in the works of Brusselle-Dupend and Cangémi (2008), Baudet et al. (2009), Shojaei and Li (2013). An other group of works considers that each phase has its own elastic strain (Bédoui et al., 2004; Zairi et al., 2011). The total inelastic strain is the average of the irreversible deformation of each phase:

$$\underline{\underline{\epsilon}}^{in} = (1 - z) \underline{\underline{\epsilon}}^a + z \underline{\underline{\epsilon}}^c \quad (5)$$

where $\underline{\underline{\epsilon}}^a$ and $\underline{\underline{\epsilon}}^c$ stand for the inelastic strain in the amorphous phase and the crystalline phase respectively. Such a decomposition has already been applied in other works (Nikolov and Doghri, 2000; Ahzi et al., 2003; van Dommelen et al., 2003; Sheng et al., 2004; Colak and Krempl, 2005).

2.1. Background of the undamaged MM model

In the MM approach, each phase is associated to a local stress tensor calculated from an appropriate stress concentration rule. For the sake of simplicity and to reduce the number of material coefficients, it is assumed in the present work that the macroscopic stress is equal to the stress in each phase.

$$\underline{\underline{\sigma}}^a = \underline{\underline{\sigma}}^c = \underline{\underline{\sigma}} = \underline{\underline{\Lambda}} : \underline{\underline{\varepsilon}}^e \quad (6)$$

This assumption of uniform stress has been successfully used for MM models in order to simulate the mechanical behavior of medium density polyethylene (BenHadj Hamouda et al., 2007) and more recently for PA6 (Cayzac et al., 2013). Note that the difference of stiffness is supported by the strains as shown by Eq. (5). Nikolov and Doghri (2000) have proposed earlier a micro-mechanical model using a static homogenization scheme for Polyethylene. The two local stresses are involved in two yield functions ϕ^a and ϕ^c defining criteria for the amorphous phase and crystalline phase respectively. The present study is only devoted to PA6 behavior under monotonic loading, the amorphous and crystalline criteria write:

$$\begin{cases} \phi^a = J(\underline{\underline{\sigma}}) - R^a - R_0^a \\ \phi^c = J(\underline{\underline{\sigma}}) - R^c - R_0^c \end{cases} \quad (7)$$

where $J(\underline{\underline{\sigma}}) = \left(\frac{3}{2} \underline{\underline{s}} : \underline{\underline{s}}\right)^{1/2}$. $\underline{\underline{s}}$ is the deviatoric part of the stress tensor. The two material parameters R_0^a and R_0^c denote the initial size of the two elastic domains, whereas R^a and R^c characterize the size change of each yield surface. They are associated to two internal variables r^a and r^c :

$$\begin{cases} R^a = b_a Q_a r^a \\ R^c = b_c Q_c r^c \end{cases} \quad (8)$$

Q_a , b_a , Q_c and b_c are isotropic hardening parameters linked to the amorphous phase and to the crystalline phase respectively. To take into account the rate sensitivity of the PA6, the model is written here in the viscoplasticity framework by introducing the material parameters K_a , n_a , K_c and n_c :

$$\begin{cases} \dot{\lambda}^a = \left\langle \frac{\phi^a}{K_a} \right\rangle^{n_a} \\ \dot{\lambda}^c = \left\langle \frac{\phi^c}{K_c} \right\rangle^{n_c} \end{cases} \quad (9)$$

The Macauley bracket $\langle \cdot \rangle$ denotes the positive part ($\langle x \rangle = 0$ if $x \leq 0$ and x otherwise). According to the normality flow rule, the viscoplastic strain rates may be expressed as:

$$\begin{cases} \dot{\underline{\underline{\varepsilon}}}^a = \dot{\lambda}^a \underline{\underline{n}}^a \quad \text{with} \quad \underline{\underline{n}}^a = \frac{3}{2} \frac{\underline{\underline{s}}}{J(\underline{\underline{\sigma}})} \\ \dot{\underline{\underline{\varepsilon}}}^c = \dot{\lambda}^c \underline{\underline{n}}^c \quad \text{with} \quad \underline{\underline{n}}^c = \frac{3}{2} \frac{\underline{\underline{s}}}{J(\underline{\underline{\sigma}})} \end{cases} \quad (10)$$

The evolution laws of the isotropic hardening variable are given by:

$$\begin{cases} \dot{r}^a = \dot{\lambda}^a \left(1 - \frac{R^a}{Q_a}\right) \\ \dot{r}^c = \dot{\lambda}^c \left(1 - \frac{R^c}{Q_c}\right) \end{cases} \quad (11)$$

2.2. Damage MM model based on GTN's approach

The most popular porous plasticity model proposed originally by Gurson (1977) is based on the concept of a plastic yield surface which is function of void volume fraction (or porosity). The

porosity evolution results from the mass conservation principle. Two MM sub-models can be distinguished:

- Since SCP consist of amorphous and crystalline phases, each phase may be characterized by its own damage variable. The total porosity is supposed to be the average of the local porosity at each phase level $f = (1 - z)f^a + zf^c$ (Sai et al., 2011). The porosity of the amorphous phase f^a and the porosity of the crystalline phase f^c are defined as follows:

$$\begin{cases} f^a = \frac{\text{cavity volume in the amorphous phase}}{\text{volume of the amorphous phase}} \\ f^c = \frac{\text{cavity volume in the crystalline phase}}{\text{volume of the crystalline phase}} \end{cases} \quad (12)$$

The related model will be referred to as ‘‘MMG2f’’.

- The damage is classically described by a unique overall variable. Indeed when damage takes place in the SCP, it cannot be attributed to one specific phase. Therefore, an overall damage variable f may be considered. It also results in a reduction of the number of damage parameters.

$$f = \frac{\text{overall cavity volume}}{\text{total volume of the material}} \quad (13)$$

This classic assumption is used in the model referred to as ‘‘MMG1f’’.

2.2.1. MM model coupled with GTN type damage ‘‘MMG2f’’

The flow potentials for the two phases are as follows:

$$\begin{cases} \phi^a = \sigma_{\star}^a - \frac{R^a}{(1-f^a)} - R_0^a \\ \phi^c = \sigma_{\star}^c - \frac{R^c}{(1-f^c)} - R_0^c \end{cases} \quad (14)$$

The effective size change of the elastic domain of each phase is affected by the damage level f^a and f^c respectively. They are related to two internal variables r^a and r^c as:

$$\begin{cases} R^a = (1-f^a)b_a Q_a r^a \\ R^c = (1-f^c)b_c Q_c r^c \end{cases} \quad (15)$$

The effective stresses σ_{\star}^a and σ_{\star}^c are implicitly founded according to Besson and Guillemer-Neel (2003) by the conditions:

$$\begin{cases} G^a(\underline{\underline{\sigma}}, f_{\star}^a, \sigma_{\star}^a) = \left(\frac{J(\underline{\underline{\sigma}})}{\sigma_{\star}^a}\right)^2 + 2q_1^a f_{\star}^a \cosh\left(\frac{q_2^a}{2} \frac{I(\underline{\underline{\sigma}})}{\sigma_{\star}^a}\right) - 1 - (q_1^a f_{\star}^a)^2 = 0 \\ G^c(\underline{\underline{\sigma}}, f_{\star}^c, \sigma_{\star}^c) = \left(\frac{J(\underline{\underline{\sigma}})}{\sigma_{\star}^c}\right)^2 + 2q_1^c f_{\star}^c \cosh\left(\frac{q_2^c}{2} \frac{I(\underline{\underline{\sigma}})}{\sigma_{\star}^c}\right) - 1 - (q_1^c f_{\star}^c)^2 = 0 \end{cases} \quad (16)$$

The material parameters q_1^a , q_2^a , q_1^c and q_2^c accounts for interactions (Faleskog et al., 1998). f_{\star}^a and f_{\star}^c are respectively functions of the porosity f^a and f^c . These two phenomenological functions account for void coalescence in the amorphous and crystalline phases.

$$f_{\star}^a = \begin{cases} f^a & \text{if } f^a < f_c^a \\ f_c^a + \delta_a(f^a - f_c^a) & \text{if } f^a \geq f_c^a \end{cases} \quad (17)$$

$$f_{\star}^c = \begin{cases} f^c & \text{if } f^c < f_c^c \\ f_c^c + \delta_c(f^c - f_c^c) & \text{if } f^c \geq f_c^c \end{cases} \quad (18)$$

where the material parameters f_c^a and f_c^c denotes the porosity at the onset of coalescence in the amorphous phase and the crystalline phase respectively. The viscoplastic strain rates are given by:

$$\begin{cases} \dot{\underline{\underline{\varepsilon}}}^a = (1-f^a)\dot{\lambda}^a \underline{\underline{n}}^a \quad \text{with} \quad \underline{\underline{n}}^a = \frac{\partial \sigma_{\star}^a}{\partial \underline{\underline{\sigma}}} \\ \dot{\underline{\underline{\varepsilon}}}^c = (1-f^c)\dot{\lambda}^c \underline{\underline{n}}^c \quad \text{with} \quad \underline{\underline{n}}^c = \frac{\partial \sigma_{\star}^c}{\partial \underline{\underline{\sigma}}} \end{cases} \quad (19)$$

According to Besson and Guillemer-Neel (2003), the derivatives with respect to stress tensor $\partial\sigma_{\star}^a/\partial\tilde{\sigma}$ and $\partial\sigma_{\star}^c/\partial\tilde{\sigma}$ are computed as:

$$\frac{\partial\sigma_{\star}^a}{\partial\tilde{\sigma}} = -\left(\frac{\partial G^a}{\partial\sigma_{\star}^a}\right)^{-1} \frac{\partial G^a}{\partial\tilde{\sigma}} \quad (20)$$

$$\frac{\partial\sigma_{\star}^c}{\partial\tilde{\sigma}} = -\left(\frac{\partial G^c}{\partial\sigma_{\star}^c}\right)^{-1} \frac{\partial G^c}{\partial\tilde{\sigma}} \quad (21)$$

Then the normal tensor to the amorphous yield surface \tilde{n}_a is defined by:

$$\begin{cases} \tilde{n}_a = P_d^a \tilde{s} + P_s^a \tilde{I} \\ P_d^a = \frac{3\sigma_{\star}}{2(J(\tilde{\sigma}))^2 + f_*^a q_1^a q_2^a I(\tilde{\sigma}) \sigma_{\star} \sinh\left(\frac{q_2^a I(\tilde{\sigma})}{2\sigma_{\star}}\right)} \\ P_s^a = \frac{q_1^a q_2^a f_*^a (\sigma_{\star})^2 \sinh\left(\frac{q_2^a I(\tilde{\sigma})}{2\sigma_{\star}}\right)}{2(J(\tilde{\sigma}))^2 + f_*^a q_1^a q_2^a I(\tilde{\sigma}) \sigma_{\star} \sinh\left(\frac{q_2^a I(\tilde{\sigma})}{2\sigma_{\star}}\right)} \end{cases} \quad (22)$$

Similarly, the normal tensor to the crystalline yield surface \tilde{n}_c is defined by:

$$\begin{cases} \tilde{n}_c = P_d^c \tilde{s} + P_s^c \tilde{I} \\ P_d^c = \frac{3\sigma_{\star}}{2(J(\tilde{\sigma}))^2 + f_*^c q_1^c q_2^c I(\tilde{\sigma}) \sigma_{\star} \sinh\left(\frac{q_2^c I(\tilde{\sigma})}{2\sigma_{\star}}\right)} \\ P_s^c = \frac{q_1^c q_2^c f_*^c (\sigma_{\star})^2 \sinh\left(\frac{q_2^c I(\tilde{\sigma})}{2\sigma_{\star}}\right)}{2(J(\tilde{\sigma}))^2 + f_*^c q_1^c q_2^c I(\tilde{\sigma}) \sigma_{\star} \sinh\left(\frac{q_2^c I(\tilde{\sigma})}{2\sigma_{\star}}\right)} \end{cases} \quad (23)$$

It is worth noting that both normals \tilde{n}^a and \tilde{n}^c are decomposed into the sum of a deviatoric part and a spherical part. The non-null spherical terms account for the volume change at the phase level and contribute to overall volume change. The evolution laws of the isotropic hardening variable write:

$$\begin{cases} \dot{j}^a = \dot{\lambda}^a \left(1 - \frac{R_a}{(1-f^a)Q_a}\right) \\ \dot{j}^c = \dot{\lambda}^c \left(1 - \frac{R_c}{(1-f^c)Q_c}\right) \end{cases} \quad (24)$$

For the PA6 under study, it is supposed that porosity are only caused by void growth. Consequently, void nucleation are “neglected” and the evolution laws of the isotropic hardening variable simply write:

$$\begin{cases} \dot{j}^a = (1-f^a)\text{Tr}(\dot{\tilde{\epsilon}}^a) \\ \dot{j}^c = (1-f^c)\text{Tr}(\dot{\tilde{\epsilon}}^c) \end{cases} \quad (25)$$

2.2.2. MM model coupled with GTN type damage “MMG1f”

As mentioned above, the damage is described by a unique overall variable porosity f .

$$f = \frac{\text{cavity volume}}{\text{total volume}} \quad (26)$$

The model of the previous section is particularized as $f^a = f^c = f$, $q_1 = q_1^a = q_1^c$ and $q_2 = q_2^a = q_2^c$. However, the evolution of the porosity due to the void growth is obtained from mass conservation.

$$\dot{f} = (1-f)\text{Tr}(\dot{\tilde{\epsilon}}^{pp}) \quad (27)$$

2.3. Damage MM model based on CDM theory

In this section, a MM model based on continuum damage mechanics is proposed to investigate the inelastic behavior of the PA6. The CDM theory supposes that the crack initiation is preceded by a progressive internal deterioration of the material (i.e. micro cracks, micro defects) which induces a loss of strength. The isotropic damage evolution is quantified by means of a macroscopic scalar variable D varying between 0 and 1 (Chaboche, 1987). The proposed model is based on the concept of effective stress and combined with a principle of energy equivalence. Similarly to the MM model based on GTN approach, two sub-models are distinguished:

- Each one of the two phases is characterized by its own damage variable: D_a for the amorphous phase and D_c for the crystalline phase. This model will be referred to as “MMC2D”. The use of two damage variables was also introduced by Boudifa et al. (2009) in micromechanical model applied to polycrystalline metals.
- Damage is classically accounted for by the mean of a unique variable D . This model will be referred to as “MMC1D”.

2.3.1. MM model coupled with CDM type damage “MMC2D”

The overall damage D is the average of the local damage of each phase:

$$D = (1-z)D^a + zD^c \quad (28)$$

In opposition to the GTN’s approach for which only the effect of the damage variable on plastic behavior is taken into account, the influence of damage is introduced into the linear elasticity behavior as well as into the plastic behavior. Accordingly, the elastic free energy writes

$$\rho\psi^e = \frac{1}{2} \left(1 - ((1-z)D^a + zD^c)\right) \left(\tilde{\epsilon}^e : \tilde{\Lambda} : \tilde{\epsilon}^e\right) \quad (29)$$

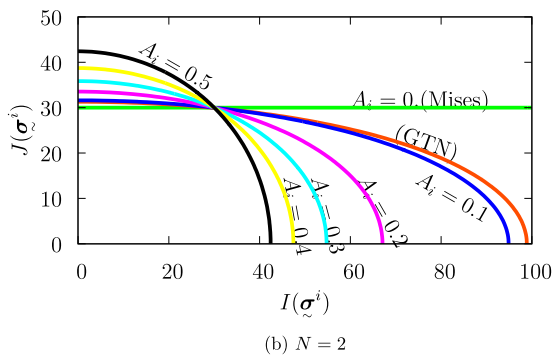
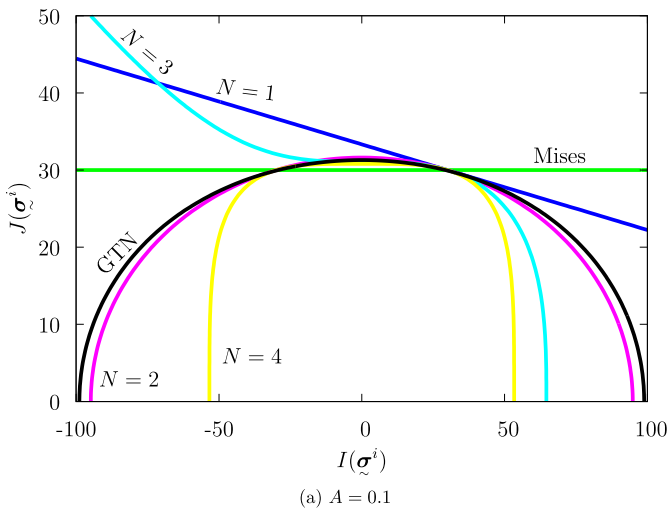


Fig. 1. Yield functions given by Eq. (37) (a) $A = 0.1$ (b) $N = 2$.

Table 1
Gurson type multi-mechanism models.

“MMG2F”	“MMG1F”
$\phi^a = \sigma_\star^a - \frac{R_a}{(1-f^a)} - R_0^a$	$\phi^a = \sigma_\star - \frac{R_a}{(1-f)} - R_0^a$
$\phi^c = \sigma_\star^c - \frac{R_c}{(1-f^c)} - R_0^c$	$\phi^c = \sigma_\star - \frac{R_c}{(1-f)} - R_0^c$
$R^a = (1-f^a)b_a Q_a r^a \quad R^c = (1-f^c)b_c Q_c r^c$	$R^a = (1-f)b_a Q_a r^a \quad R^c = (1-f)b_c Q_c r^c$
$G^a(J(\underline{\sigma}), \sigma_\star^a, f^a) = \left(\frac{J(\underline{\sigma})}{\sigma_\star^a}\right)^2 +$	$G(J(\underline{\sigma}), \sigma_\star, f) = \left(\frac{J(\underline{\sigma})}{\sigma_\star}\right)^2 +$
$2q_1^a f^a \cosh\left(\frac{q_2^a I(\underline{\sigma})}{2\sigma_\star^a}\right) - 1 - (q_1^a f^a)^2 = 0$	$2q_1 f \cosh\left(\frac{q_2 I(\underline{\sigma})}{2\sigma_\star}\right) - 1 - (q_1 f)^2 = 0$
$G^c(J(\underline{\sigma}), \sigma_\star^c, f^c) = \left(\frac{J(\underline{\sigma})}{\sigma_\star^c}\right)^2 +$	
$2q_1^c f^c \cosh\left(\frac{q_2^c I(\underline{\sigma})}{2\sigma_\star^c}\right) - 1 - (q_1^c f^c)^2 = 0$	
$\dot{\lambda}^a = \left\langle \frac{\phi^a}{K_a} \right\rangle^{n_a} \quad \dot{\lambda}^c = \left\langle \frac{\phi^c}{K_c} \right\rangle^{n_c}$	$\dot{\lambda}^a = \left\langle \frac{\phi^a}{K_a} \right\rangle^{n_a} \quad \dot{\lambda}^c = \left\langle \frac{\phi^c}{K_c} \right\rangle^{n_c}$
$\dot{\underline{\epsilon}}^a = (1-f^a)\dot{\lambda}^a \underline{\mathbf{n}}^a \quad \dot{\underline{\epsilon}}^c = (1-f^c)\dot{\lambda}^c \underline{\mathbf{n}}^c$	$\dot{\underline{\epsilon}}^a = (1-f)\dot{\lambda}^a \underline{\mathbf{n}} \quad \dot{\underline{\epsilon}}^c = (1-f)\dot{\lambda}^c \underline{\mathbf{n}}$
$\underline{\mathbf{n}}^a = P_d^a \underline{\mathbf{s}} + P_s^a \underline{\mathbf{I}} \quad \underline{\mathbf{n}}^c = P_d^c \underline{\mathbf{s}} + P_s^c \underline{\mathbf{I}}$	$\underline{\mathbf{n}} = P_d \underline{\mathbf{s}} + P_s \underline{\mathbf{I}}$
$P_d^a = \frac{3\sigma_\star^a}{2(J(\underline{\sigma}))^2 + f^a q_1^a q_2^a I(\underline{\sigma}) \sigma_\star^a \sinh\left(\frac{q_2^a I(\underline{\sigma})}{2\sigma_\star^a}\right)}$	$P_d = \frac{3\sigma_\star}{2(J(\underline{\sigma}))^2 + f q_1 q_2 I(\underline{\sigma}) \sigma_\star \sinh\left(\frac{q_2 I(\underline{\sigma})}{2\sigma_\star}\right)}$
$P_d^c = \frac{3\sigma_\star^c}{2(J(\underline{\sigma}))^2 + f^c q_1^c q_2^c I(\underline{\sigma}) \sigma_\star^c \sinh\left(\frac{q_2^c I(\underline{\sigma})}{2\sigma_\star^c}\right)}$	
$P_s^a = \frac{q_1^a q_2^a (\sigma_\star^a)^2 \sinh\left(\frac{q_2^a I(\underline{\sigma})}{2\sigma_\star^a}\right)}{2(J(\underline{\sigma}))^2 + f^a q_1^a q_2^a I(\underline{\sigma}) \sigma_\star^a \sinh\left(\frac{q_2^a I(\underline{\sigma})}{2\sigma_\star^a}\right)}$	$P_s = \frac{q_1 q_2 (\sigma_\star)^2 \sinh\left(\frac{q_2 I(\underline{\sigma})}{2\sigma_\star}\right)}{2(J(\underline{\sigma}))^2 + f q_1 q_2 I(\underline{\sigma}) \sigma_\star \sinh\left(\frac{q_2 I(\underline{\sigma})}{2\sigma_\star}\right)}$
$P_s^c = \frac{q_1^c q_2^c (\sigma_\star^c)^2 \sinh\left(\frac{q_2^c I(\underline{\sigma})}{2\sigma_\star^c}\right)}{2(J(\underline{\sigma}))^2 + f^c q_1^c q_2^c I(\underline{\sigma}) \sigma_\star^c \sinh\left(\frac{q_2^c I(\underline{\sigma})}{2\sigma_\star^c}\right)}$	
$\dot{r}^a = \dot{\lambda}^a \left(1 - \frac{R^a}{(1-f^a)Q_a}\right)$	$\dot{r}^a = \dot{\lambda}^a \left(1 - \frac{R^a}{(1-f)Q_a}\right)$
$\dot{r}^c = \dot{\lambda}^c \left(1 - \frac{R^c}{(1-f^c)Q_c}\right)$	$\dot{r}^c = \dot{\lambda}^c \left(1 - \frac{R^c}{(1-f)Q_c}\right)$
$\dot{f}^a = (1-f^a)\text{Tr}(\dot{\underline{\epsilon}}^a) \quad \dot{f}^c = (1-f^c)\text{Tr}(\dot{\underline{\epsilon}}^c)$	$\dot{f} = (1-f)\text{Tr}(\dot{\underline{\epsilon}})$

Table 2
CDM based multi-mechanism models.

“MMC2D”	“MMC1D”
$\phi^a = \frac{1}{\sqrt{(1-D^a)}} (\sigma_{eq}^a - R^a) - R_0^a$	$\phi^a = \frac{1}{\sqrt{(1-D)}} (\sigma_{eq} - R_a) - R_0^a$
$\phi^c = \frac{1}{\sqrt{(1-D^c)}} (\sigma_{eq}^c - R^c) - R_0^c$	$\phi^c = \frac{1}{\sqrt{(1-D)}} (\sigma_{eq} - R_c) - R_0^c$
$\sigma_{eq}^a = \left((1-A_a)(J(\underline{\sigma}))^N + A_a(I(\underline{\sigma}))^N \right)^{\frac{1}{N}}$	$\sigma_{eq} = \left((1-A)(J(\underline{\sigma}))^N + A(I(\underline{\sigma}))^N \right)^{\frac{1}{N}}$
$\sigma_{eq}^c = \left((1-A_c)(J(\underline{\sigma}))^N + A_c(I(\underline{\sigma}))^N \right)^{\frac{1}{N}}$	
$\underline{\sigma} \approx (1 - ((1-z)D_a + zD_c)) \underline{\Lambda} : \underline{\epsilon}^e$	$\underline{\sigma} = (1-D) \underline{\Lambda} : \underline{\epsilon}^e$
$R^a = (1-D_a)b_a Q_a r^a \quad R^c = (1-D_c)b_c Q_c r^c$	$R_a = (1-D)b_a Q_a r^a \quad R_c = (1-D)b_c Q_c r^c$
$Y^e = \frac{1}{2}(1-z)(\underline{\epsilon}^e : \underline{\Lambda} : \underline{\epsilon}^e) \quad Y_c^e = \frac{1}{2}z(\underline{\epsilon}^e : \underline{\Lambda} : \underline{\epsilon}^e)$	$Y^e = \frac{1}{2}(\underline{\epsilon}^e : \underline{\Lambda} : \underline{\epsilon}^e)$
$Y^{vp} = \frac{1}{2}b_a Q_a (r^a)^2 \quad Y_c^{vp} = \frac{1}{2}b_c Q_c (r^c)^2$	$Y^{vp} = \frac{1}{2}b_a Q_a (r^a)^2 + \frac{1}{2}b_c Q_c (r^c)^2$
$Y^a = Y_a^e + Y_a^{vp} \quad Y^c = Y_c^e + Y_c^{vp}$	$Y = Y^e + Y^{vp}$
$\dot{\underline{\epsilon}}^a = \dot{\lambda}^a \frac{1}{\sqrt{(1-D_a)}} \underline{\mathbf{n}}^a \quad \dot{\underline{\epsilon}}^c = \dot{\lambda}^c \frac{1}{\sqrt{(1-D_c)}} \underline{\mathbf{n}}^c$	$\dot{\underline{\epsilon}}^a = \dot{\lambda}^a \frac{1}{\sqrt{(1-D)}} \underline{\mathbf{n}} \quad \dot{\underline{\epsilon}}^c = \dot{\lambda}^c \frac{1}{\sqrt{(1-D)}} \underline{\mathbf{n}}$
$\dot{\lambda}^a = \left\langle \frac{\phi^a}{K_a} \right\rangle^{n^a} \quad \dot{\lambda}^c = \left\langle \frac{\phi^c}{K_c} \right\rangle^{n^c}$	$\dot{\lambda}^a = \left\langle \frac{\phi^a}{K_a} \right\rangle^{n^a} \quad \dot{\lambda}^c = \left\langle \frac{\phi^c}{K_c} \right\rangle^{n^c}$
$\underline{\mathbf{n}}^a = \frac{(\sigma_{eq}^a)^{\frac{1}{N}-1}}{\sqrt{(1-D^a)}} \left(\frac{3}{2}(1-A_a)(J(\underline{\sigma}))^{(N-2)} \underline{\mathbf{s}} + A_a(I(\underline{\sigma}))^{(N-1)} \underline{\mathbf{I}} \right)$	$\underline{\mathbf{n}} = \frac{(\sigma_{eq})^{\frac{1}{N}-1}}{\sqrt{(1-D)}} \left(\frac{3}{2}(1-A)(J(\underline{\sigma}))^{(N-2)} \underline{\mathbf{s}} + A(I(\underline{\sigma}))^{(N-1)} \underline{\mathbf{I}} \right)$
$\underline{\mathbf{n}}^c = \frac{(\sigma_{eq}^c)^{\frac{1}{N}-1}}{\sqrt{(1-D^c)}} \left(\frac{3}{2}(1-A_c)(J(\underline{\sigma}))^{(N-2)} \underline{\mathbf{s}} + A_c(I(\underline{\sigma}))^{(N-1)} \underline{\mathbf{I}} \right)$	
$\dot{r}^a = \dot{\lambda}^a \left(\frac{1}{\sqrt{(1-D^a)}} - \frac{R^a}{(1-D^a)Q_a} \right)$	$\dot{r}^a = \dot{\lambda}^a \left(\frac{1}{\sqrt{(1-D)}} - \frac{R^a}{(1-D)Q_a} \right)$
$\dot{r}^c = \dot{\lambda}^c \left(\frac{1}{\sqrt{(1-D^c)}} - \frac{R^c}{(1-D^c)Q_c} \right)$	$\dot{r}^c = \dot{\lambda}^c \left(\frac{1}{\sqrt{(1-D)}} - \frac{R^c}{(1-D)Q_c} \right)$
$\dot{D}^a = \dot{\lambda}^a \left(\frac{Y^a}{S_a} \right)^{S_a} \quad \dot{D}^c = \dot{\lambda}^c \left(\frac{Y^c}{S_c} \right)^{S_c}$	$\dot{D} = ((1-z)\dot{\lambda}^a + z\dot{\lambda}^c) \left(\frac{Y}{S} \right)^S$

Table 3
Identified parameters for the “undamaged” PA6.

	Isotropic hardening			Norton law	
	R_0^a	b_a	Q_a	n_a	K_a
Amorphous	25	4.4	95	2.5	250
Crystalline	R_0^c	b_c	Q_c	n_c	K_c
	3	3.8	110	5	800

The overall stress tensor is then deduced:

$$\tilde{\sigma} = (1 - ((1 - z)D^a + zD^c)) \tilde{\Lambda} : \tilde{\epsilon}^e \quad (30)$$

In the viscoplastic free energy, the two phases are supposed to be affected by damage:

$$\rho\psi^{vp} = \frac{1}{2}b_aQ_a(1 - D^a)(r^a)^2 + \frac{1}{2}b_cQ_c(1 - D^c)(r^c)^2 \quad (31)$$

In these conditions, the size change of the two elastic domain are as follows:

$$\begin{cases} R^a = (1 - D^a)b_aQ_a r^a \\ R^c = (1 - D^c)b_cQ_c r^c \end{cases} \quad (32)$$

The elastic thermodynamic forces Y_a^e and Y_c^e associated respectively with damage variables D^a and D^c are given by:

$$\begin{cases} Y_a^e = -\rho \frac{\partial \psi^e}{\partial D^a} = \frac{1}{2}(1 - z)(\tilde{\epsilon}^e : \tilde{\Lambda} : \tilde{\epsilon}^e) \\ Y_c^e = -\rho \frac{\partial \psi^e}{\partial D^c} = \frac{1}{2}z(\tilde{\epsilon}^e : \tilde{\Lambda} : \tilde{\epsilon}^e) \end{cases} \quad (33)$$

Similarly, the viscoplastic thermodynamic forces Y_{vp}^a and Y_{vp}^c write:

$$\begin{cases} Y_a^{vp} = -\rho \frac{\partial \psi^{vp}}{\partial D^a} = \frac{1}{2}b_aQ_a(r^a)^2 \\ Y_c^{vp} = -\rho \frac{\partial \psi^{vp}}{\partial D^c} = \frac{1}{2}b_cQ_c(r^c)^2 \end{cases} \quad (34)$$

The overall thermodynamic forces Y^a and Y^c associated with D^a and D^c are the sum of the two previous thermodynamic forces:

$$\begin{cases} Y^a = Y_a^e + Y_a^{vp} = \frac{1}{2}(1 - z)(\tilde{\epsilon}^e : \tilde{\Lambda} : \tilde{\epsilon}^e) + \frac{1}{2}b_aQ_a(r^a)^2 \\ Y^c = Y_c^e + Y_c^{vp} = \frac{1}{2}z(\tilde{\epsilon}^e : \tilde{\Lambda} : \tilde{\epsilon}^e) + \frac{1}{2}b_cQ_c(r^c)^2 \end{cases} \quad (35)$$

In order to allow the description of the damage-induced plastic volume variation or compressibility as in the GTN's approach, the two yield criteria can be expressed following (Chaboche et al., 2006) as:

$$\begin{cases} \phi^a = \frac{1}{\sqrt{(1 - D^a)}} (\sigma_{eq}^a - R^a) - R_0^a \\ \phi^c = \frac{1}{\sqrt{(1 - D^c)}} (\sigma_{eq}^c - R^c) - R_0^c \end{cases} \quad (36)$$

σ_{eq} is a combination of the second and the first invariant of the stress tensor:

$$\begin{cases} \sigma_{eq}^a = \left((1 - A_a)(J(\tilde{\sigma}))^N + A_a(I(\tilde{\sigma}))^N \right)^{\frac{1}{N}} \\ \sigma_{eq}^c = \left((1 - A_c)(J(\tilde{\sigma}))^N + A_c(I(\tilde{\sigma}))^N \right)^{\frac{1}{N}} \end{cases} \quad (37)$$

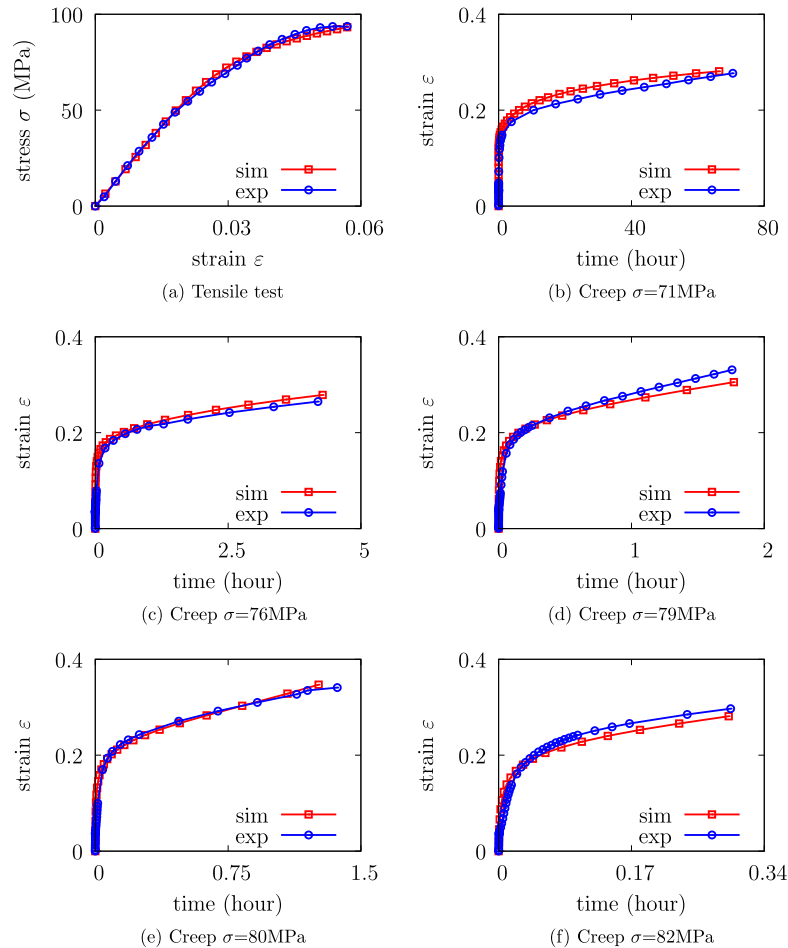


Fig. 2. Comparison of the experimental response and simulation of the tensile and creep tests.

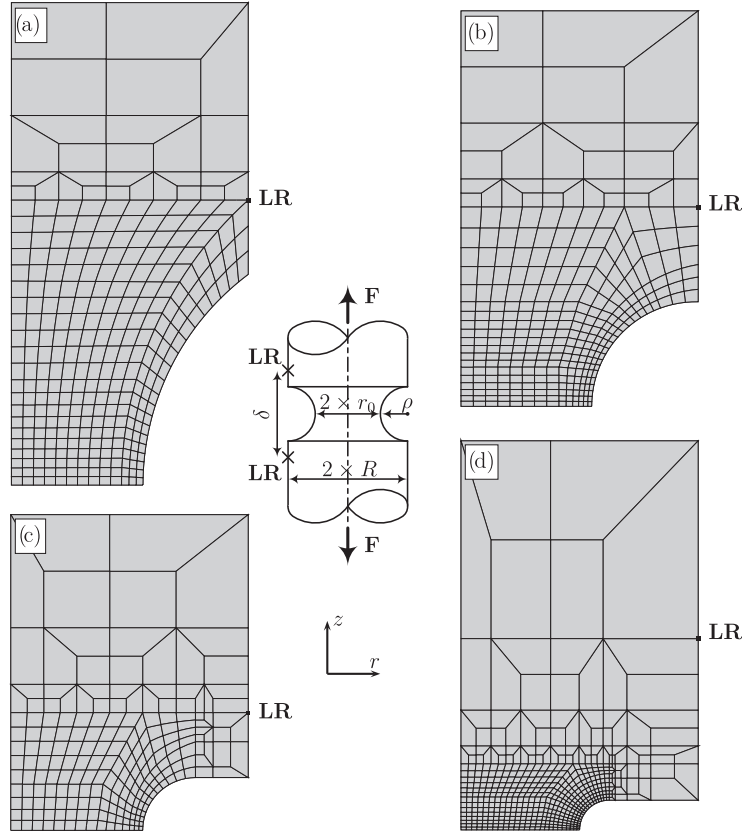


Fig. 3. Meshes of notched round bars with $R = 3.6$ mm and $r_0 = 1.8$ mm for all specimens: (a) Notched round bars with $\rho = 4$ mm, (b) $\rho = 1.6$ mm, (c) $\rho = 0.8$ mm, (d) $\rho = 0.45$ mm, LR position of laser reflector.

A parametric study is shown in Fig. 1 to illustrate typical yield criteria given by Eq. (37) for various values of parameter N and A_i ($i = a$ or c). It can be seen that GTN's model can be (almost) recovered by $N = 2$ and $A_i = 0.1$. It should be expected that the macroscopic results provided by the MM coupled with GTN and the MM coupled with CDM theory might be substantially close. The two normal to the yield surface of the amorphous phase and the crystalline phase can be calculated as:

$$\begin{cases} \tilde{\mathbf{n}}^a = \frac{J(\tilde{\boldsymbol{\sigma}})^{\frac{1}{N-1}}}{\sqrt{(1-D^a)}} \left(\frac{3}{2}(1-A_a)J(\tilde{\boldsymbol{\sigma}})^{(N-2)} \tilde{\mathbf{s}} + A_a I(\tilde{\boldsymbol{\sigma}})^{(N-1)} \tilde{\mathbf{I}} \right) \\ \tilde{\mathbf{n}}^c = \frac{J(\tilde{\boldsymbol{\sigma}})^{\frac{1}{N-1}}}{\sqrt{(1-D^c)}} \left(\frac{3}{2}(1-A_c)J(\tilde{\boldsymbol{\sigma}})^{(N-2)} \tilde{\mathbf{s}} + A_c I(\tilde{\boldsymbol{\sigma}})^{(N-1)} \tilde{\mathbf{I}} \right) \end{cases} \quad (38)$$

In this formulation, a classic version of the Drucker–Prager model is recovered by choosing $N = 1$. Finally, the evolution laws of the isotropic hardening variable and the damage variables are:

$$\begin{cases} \dot{r}^a = \dot{\lambda}^a \left(\frac{1}{\sqrt{(1-D^a)}} - \frac{R^a}{(1-D^a)Q_a} \right) \\ \dot{r}^c = \dot{\lambda}^c \left(\frac{1}{\sqrt{(1-D^c)}} - \frac{R^c}{(1-D^c)Q_c} \right) \\ \dot{D}^a = \dot{\lambda}^a \left(\frac{Y^a}{S_a} \right)^{S_a} \\ \dot{D}^c = \dot{\lambda}^c \left(\frac{Y^c}{S_c} \right)^{S_c} \end{cases} \quad (39)$$

2.3.2. MM model coupled with CDM type damage “MMC1D”

By comparing to the model detailed in the previous section, a simplified version might be obtained by considering an overall damage variable D associated to a thermodynamical force Y . In such a case, damage is described by two material parameters s and S . In the same way, the volume change is controlled by a single

parameter A . The so called “MMC1D” model can be considered as a particular case of the model “MMC2D” by choosing $S_a = S_c = S$, $s_a = s_c = s$ and $A_a = A_c = A$. The elastic thermodynamic force writes:

$$Y^e = \frac{1}{2} (\tilde{\boldsymbol{\varepsilon}}^e : \tilde{\boldsymbol{\Lambda}} : \tilde{\boldsymbol{\varepsilon}}^e) \quad (40)$$

Similarly, the viscoplastic thermodynamic forces Y_{vp}^a and Y_{vp}^c write:

$$Y_{vp} = \frac{1}{2} b_a Q_a (r_a)^2 + \frac{1}{2} b_c Q_c (r^c)^2 \quad (41)$$

The overall thermodynamic forces Y associated with D is the sum of the two previous thermodynamic forces:

$$Y = Y^e + Y_{vp} = \frac{1}{2} (1-z) (\tilde{\boldsymbol{\varepsilon}}^e : \tilde{\boldsymbol{\Lambda}} : \tilde{\boldsymbol{\varepsilon}}^e) + \frac{1}{2} b_a Q_a (r^a)^2 \quad (42)$$

In these conditions the evolution of the damage variable D is given by:

$$\dot{D} = \left((1-z) \dot{\lambda}^a + z \dot{\lambda}^c \right) \left(\frac{Y}{S} \right)^s \quad (43)$$

Table 4

Identified parameters for the damage behavior of the PA6.

Model “MMG2f”	$q_1^a = 1.785$	$q_2^a = 1.34$	$\delta_a = 0$	$q_1^c = 2.68$	$q_2^c = 1.4$	$\delta_c = 0$
Model “MMG1f”	$q_1 = 1.77$	$q_2 = 1.25$	$\delta = 0$			
Model “MMC2D”	$S_a = 6.9$	$s_a = 2.7$	$A_a = 0.025$	$S_c = 4.5$	$s_c = 3.0$	$A_c = 0.025$
Model “MMC1D”	$S = 10$	$s = 3$	$A = 0.065$			

Table 5
Initial porosity/damage for the different models.

Radius	Loading	“MMG2f”	“MMC1f”	“MMC2D”	“MMC1D”
$\rho = 4.0 \text{ mm}$	$\sigma = 70 \text{ MPa}$	$f_0^a = f_0^c = 1.22\%$	$f = 1.22\%$	$D_0^a = D_0^c = 0.0806$	$D = 0.0806$
	$\sigma = 74 \text{ MPa}$	$f_0^a = f_0^c = 1.30\%$	$f = 1.30\%$	$D_0^a = D_0^c = 0.0566$	$D = 0.0566$
	$\sigma = 78 \text{ MPa}$	$f_0^a = f_0^c = 2.25\%$	$f = 2.25\%$	$D_0^a = D_0^c = 0.1132$	$D = 0.1132$
$\rho = 1.6 \text{ mm}$	$\sigma = 70 \text{ MPa}$	$f_0^a = f_0^c = 1.92\%$	$f = 1.92\%$	$D_0^a = D_0^c = 0.1768$	$D = 0.1768$
	$\sigma = 74 \text{ MPa}$	$f_0^a = f_0^c = 2.14\%$	$f = 2.14\%$	$D_0^a = D_0^c = 0.1716$	$D = 0.1716$
	$\sigma = 78 \text{ MPa}$	$f_0^a = f_0^c = 2.08\%$	$f = 2.08\%$	$D_0^a = D_0^c = 0.1580$	$D = 0.1580$
$\rho = 0.8 \text{ mm}$	$\sigma = 70 \text{ MPa}$	$f_0^a = f_0^c = 2.00\%$	$f = 2.00\%$	$D_0^a = D_0^c = 0.2040$	$D = 0.2040$
	$\sigma = 74 \text{ MPa}$	$f_0^a = f_0^c = 1.90\%$	$f = 1.90\%$	$D_0^a = D_0^c = 0.1641$	$D = 0.1641$
	$\sigma = 78 \text{ MPa}$	$f_0^a = f_0^c = 1.68\%$	$f = 1.68\%$	$D_0^a = D_0^c = 0.1391$	$D = 0.1391$
$\rho = 0.45 \text{ mm}$	$\sigma = 70 \text{ MPa}$	$f_0^a = f_0^c = 0.68\%$	$f = 0.68\%$	$D_0^a = D_0^c = 0.1000$	$D = 0.1000$
	$\sigma = 73 \text{ MPa}$	$f_0^a = f_0^c = 0.97\%$	$f = 0.97\%$	$D_0^a = D_0^c = 0.0970$	$D = 0.0970$
	$\sigma = 80 \text{ MPa}$	$f_0^a = f_0^c = 1.11\%$	$f = 1.11\%$	$D_0^a = D_0^c = 0.0802$	$D = 0.0802$

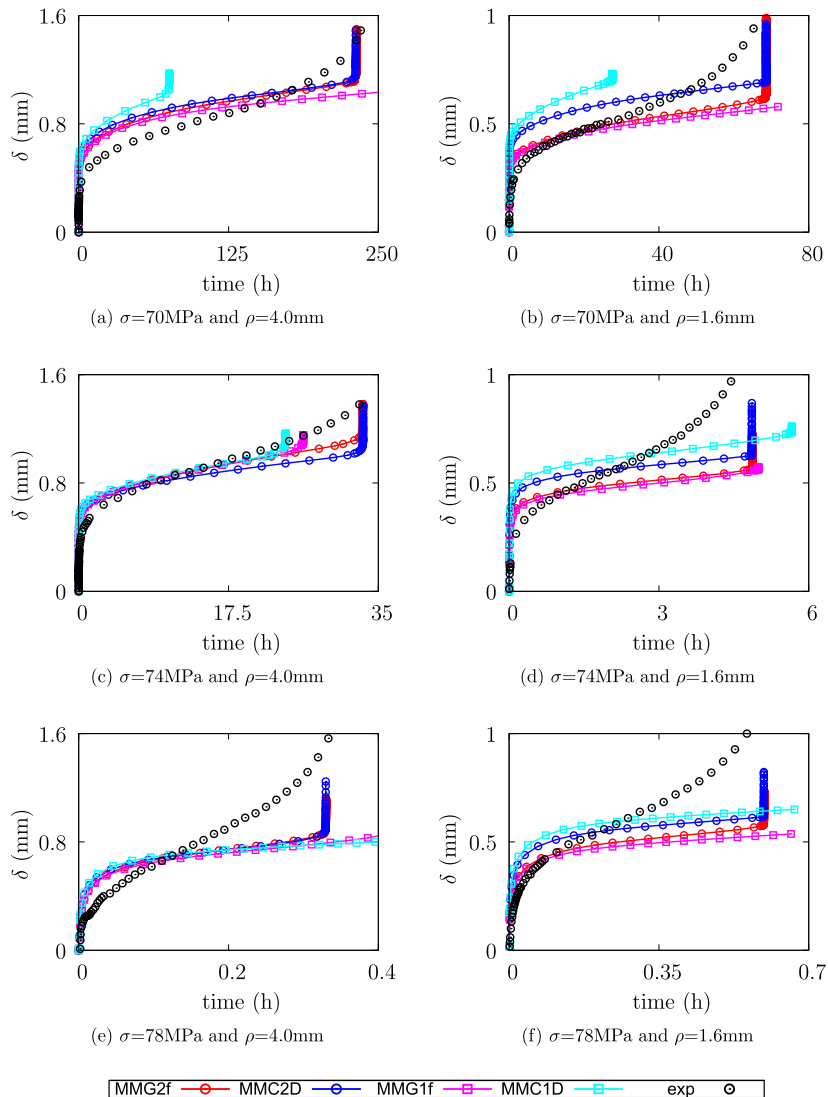


Fig. 4. Creep tests used for the identification of the damage parameters ($\rho = 4 \text{ mm}$ and 1.6 mm) – notched specimen.

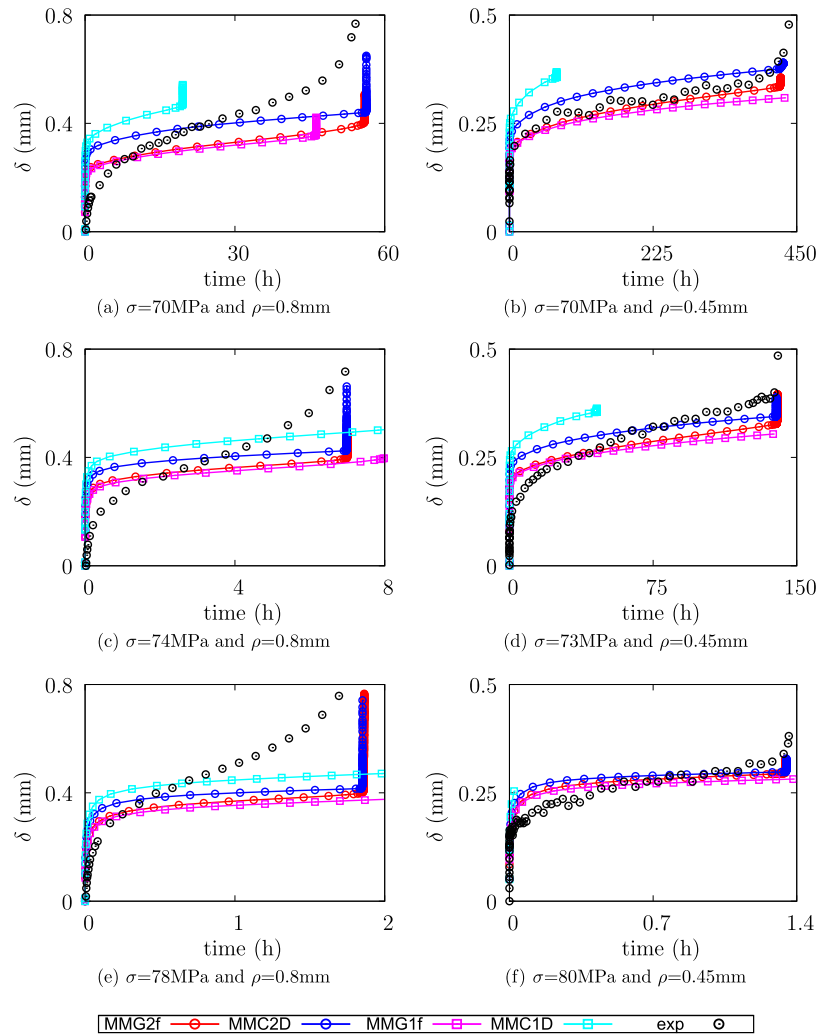


Fig. 5. Creep tests used for the identification of the damage parameters ($\rho = 0.8 \text{ mm}$ and 0.45 mm) – notched specimen (Continued).

Table 6
Initial NODs (δ_0) for the different specimens.

Radius	Loading	NOD (δ_0)
$\rho = 4.0 \text{ mm}$	$\sigma = 70 \text{ MPa}$	8.085 mm
	$\sigma = 74 \text{ MPa}$	8.654 mm
	$\sigma = 78 \text{ MPa}$	8.239 mm
$\rho = 1.6 \text{ mm}$	$\sigma = 70 \text{ MPa}$	5.263 mm
	$\sigma = 74 \text{ MPa}$	6.097 mm
	$\sigma = 78 \text{ MPa}$	6.504 mm
$\rho = 0.8 \text{ mm}$	$\sigma = 70 \text{ MPa}$	4.198 mm
	$\sigma = 74 \text{ MPa}$	3.566 mm
	$\sigma = 78 \text{ MPa}$	3.530 mm
$\rho = 0.45 \text{ mm}$	$\sigma = 70 \text{ MPa}$	8.500 mm
	$\sigma = 73 \text{ MPa}$	5.800 mm
	$\sigma = 80 \text{ MPa}$	6.500 mm

The detailed equations of the MM model coupled with GTN type damage and the MM model coupled with the CDM theory are summarized in Tables 1 and 2, respectively.

3. Results

In the previous section, Eqs. (4)–(43) display some material coefficients that have to be determined (see also Tables 1 and 2). Identification of these parameters was performed using the following procedure:

- Tensile and creep tests performed on smooth specimen are first used to identify the material parameters of the “undamaged material” common to all four models. The strain rate was of 0.026 s^{-1} for the tensile test and the creep tests are performed at the following load levels (71, 76, 79, 80, 82 MPa).
- Creep tests carried out on notched specimen are then used for the determination of the material parameters dedicated to characterize the damage behavior. A first selection of models is made on this basis.
- Numerical results are finally analyzed to check the relevance of the selected models and to retain the more predictive model.

3.1. Identification of the material parameters of the “undamaged material” (smooth specimen)

First, damage were deactivated in order to focus only on the undamaged model coefficients obtained from smooth specimens. The apparent Young’s elastic modulus have been already determined in the work of Regrain et al. (2009). It is checked here by calculating the initial slope of the stress–strain curve and set up to 2800 MPa. Poisson’s ratio is assigned to $\nu = 0.38$. The identification process of the remaining parameters has conducted to following two main steps:

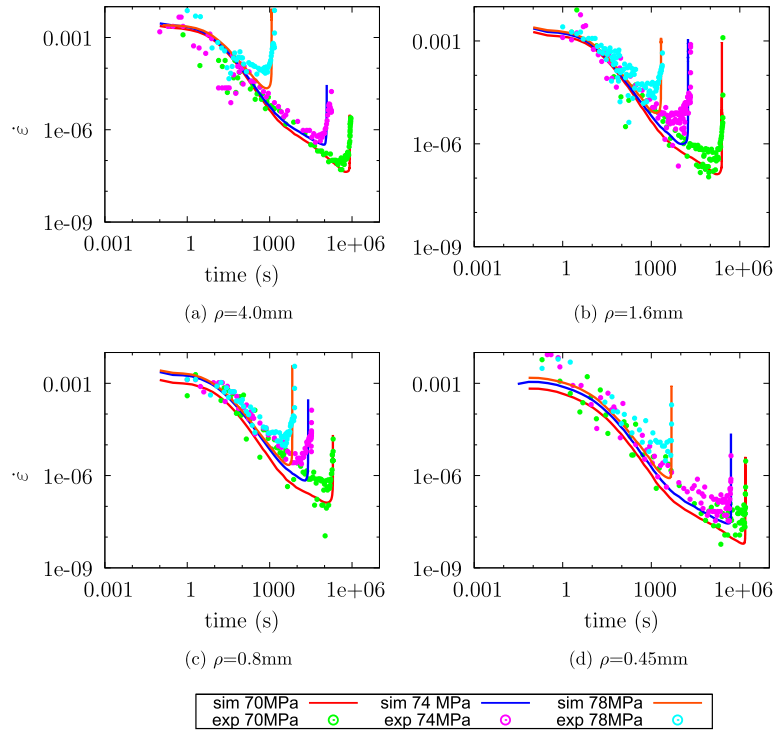


Fig. 6. Simulated (with “MMC2D” and “MMG2f” models) and experimental creep rates for the notched specimens.

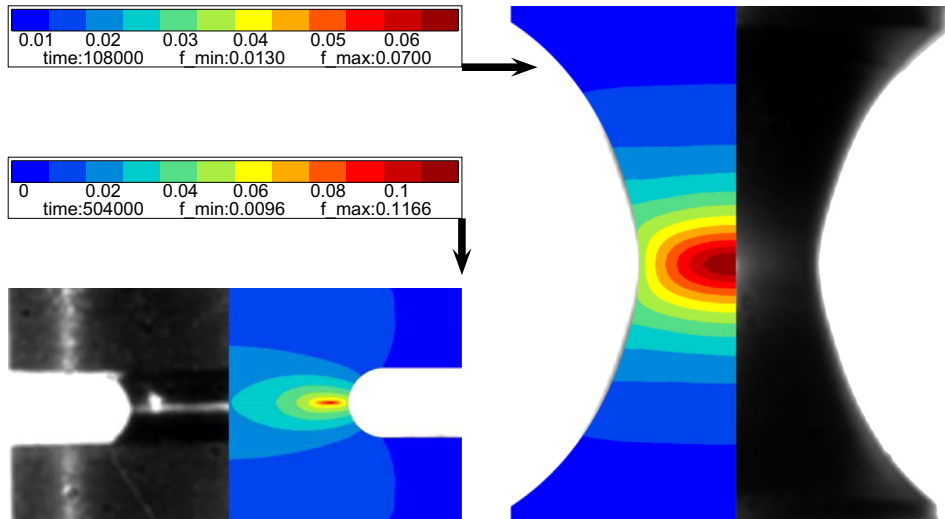


Fig. 7. Contour plot of the porosity predicted by the model “MMG2f” at the beginning of the tertiary creep stage (108,000 s for $\rho = 4$ mm, 504,000 s for $\rho = 0.45$ mm).

- The first step of the optimization procedure is devoted to the determination of the material parameters of the amorphous phase which deals with short time effect. Crystalline phase seems not to produce creep strain during tensile tests. Therefore, only the mechanism associated to the amorphous phase is activated. A big value is assigned to the initial size of the elastic domain for mechanism of the crystalline phase. The parameters n_a , K_a , Q_a , b_a , and R_0^a are first identified. The non-linear behavior of the amorphous phase is mainly obtained by the material parameter n_a . Tensile tests show that this non-linearity was not pronounced enough, so that n_a is estimated at 2.5. The value of yield stress is estimated graphically

when the stress–strain curve deviates from linear to nonlinear regime (≈ 40 MPa). R_0^a is assigned arbitrarily to 20 MPa to ensure to the mechanism of the amorphous phase to take over and replace the elastic behavior. The evaluation of the remaining parameters K_a , Q_a , b_a is then performed through an optimization process.

- The second step of the optimization procedure deals with the optimization of the parameters of the crystalline phase supposed to deal with long time effect encountered in the creep tests. To be in agreement with the time dependent phenomena, n_c is approximately set to $2 \times n_a \approx 5$. R_0^c is constrained at a small value less than 10 MPa. In this step, when it is necessary, some

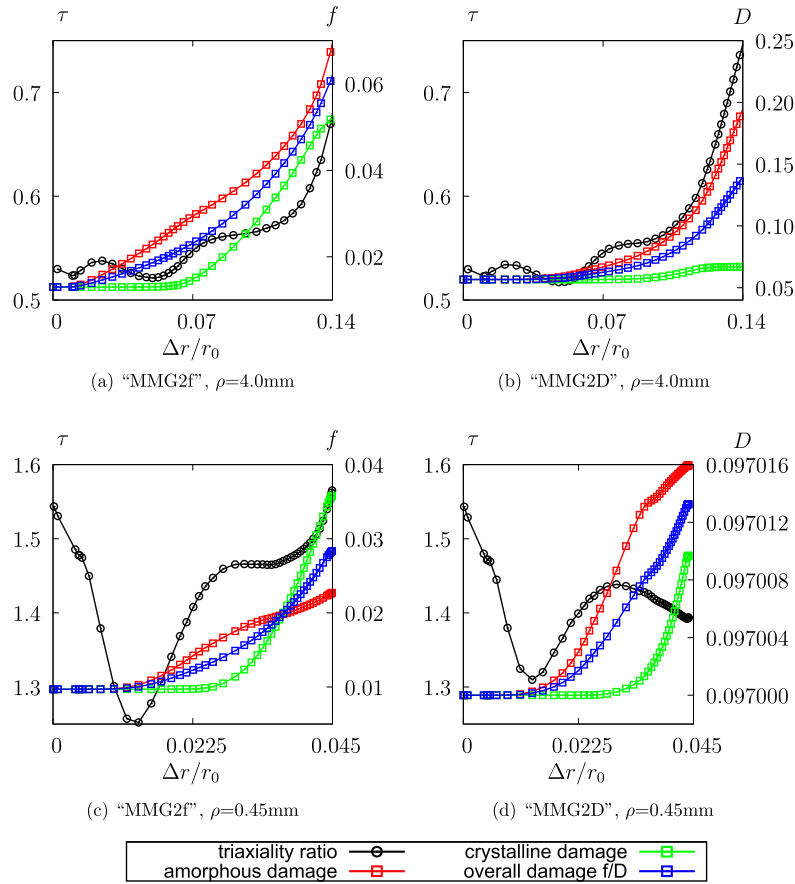


Fig. 8. Damage variables versus radial strain curves of two notch radii $\rho = 4.0$ mm and $\rho = 0.45$ mm for both “MMG2f” and “MMC2D” models for $\sigma = 74$ MPa.

of the parameters estimated in the first step were adjusted in order to enable better representation of the experimental tensile curves.

The material parameters are numerically identified by means of the optimization module of the software Zset (Besson et al., 1998) with a sequential quadratic programming (SQP) method (Stoer, 1985). This optimization method is suitable when minimizing the deviation between experimental data and simulated tests when the simulation is near the experiments. It also allows to include constraint conditions that relate the different parameters. The list of the calibrated coefficients for the MM models is given in Table 3 and the corresponding comparison between simulated responses and experimental tensile and creep data are shown in Fig. 2. Since this first stage is only focused on the determination of undamaged model coefficients, the simulations were intentionally interrupted before necking occurs (after 6% for the tensile test and at the end of secondary creep for the creep tests). For the sake of clarity, the creep tests (Figs. 2b–f) are shown in separate plots. Indeed, as the load level increases the time of the end of secondary creep decreases. The MM model is able to reproduce both short (tensile test) and long term creep strain history of the PA6 thanks to the opportunity allowed by the MM model to separate the two different behaviors in the constitutive equations. It is worth noting that only 10 parameters are used for the undamaged material. In the next section, these parameters will be kept unchanged. Notched specimen devoted to characterize the damage behavior will then be used to identify the remaining material parameters. The four models “MMG2f”, “MMC2D”, “MMG1f” and “MMC1D” will therefore be evaluated in predicting creep behaviors of notched specimens with different notch radii. The experimental responses used in

evaluating the proposed include result taken from Cayzac et al. (2013) and new experiments performed in the present work.

3.2. Identification of the material parameters of the “damaged material” (notched specimen)

The material parameters (Table 3) identified using tensile and creep tests performed on smooth specimens parameters will not be further modified. In order to validate the predictive capabilities of the proposed theory and its numerical implementation, finite element simulations of notched specimens subjected to creep behavior are used to evaluate the remainder of material parameters that characterize the damage behavior. Multiaxial specimens consisting of notched round bars with machined notch root radii ($\rho = 0.45, 0.8, 1.6$ and 4 mm) are used for that purpose. Specimens with a sharper notch radius ($\rho = 0.45, 0.8$ mm) are used to check the accuracy of the model for high stress triaxiality ratio where the ductility loss is greatest. The larger notch depths ($\rho = 1.6$ and 4 mm) are devoted to study the model capability to account for low stress triaxiality ratio. Computations were performed thanks to the finite element code Zset. For all the geometries, axisymmetrical elements with reduced integration were used with updated Lagrangian formulation under finite strain. Only one-quarter of the geometry are meshed as illustrated in Fig. 3. Distributed loads corresponding to the experimental one is imposed on the top node sets. A node located at the position of the laser beam reflector “LR” was selected to follow the creep notch opening displacement (NOD), δ . Four stress creep levels (70, 74, 78 and 80 MPa) were considered to evaluate the prediction of the NOD for the four considered models. The material parameters were adjusted “manually” in order to enable better representation of the tertiary creep. In

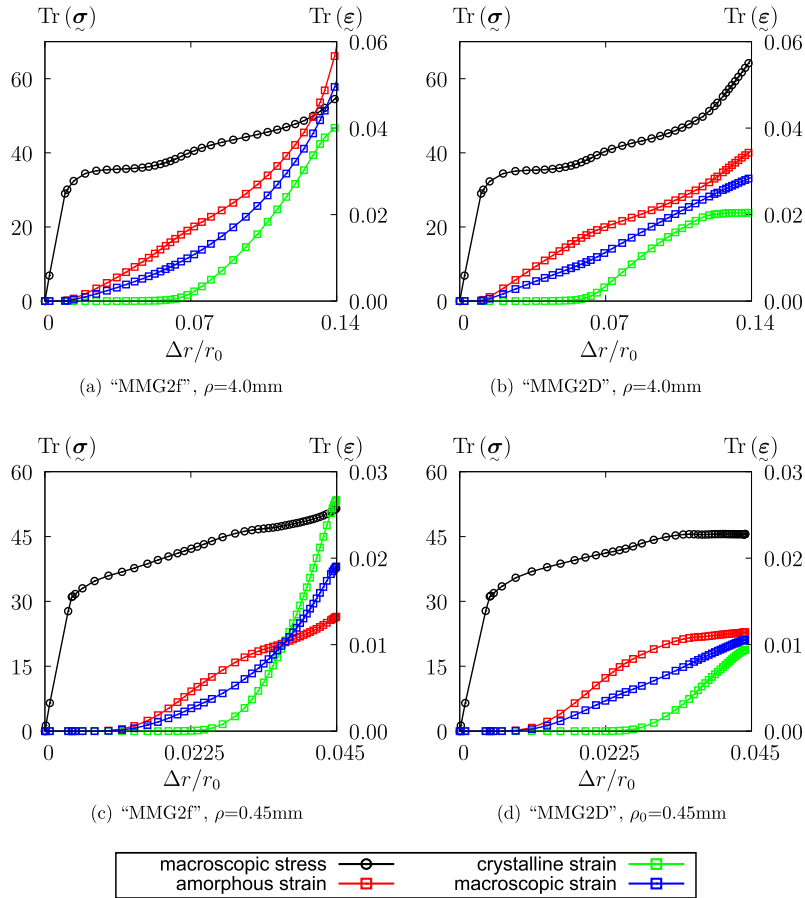


Fig. 9. Stress and strain versus strain of two notch radii $\rho = 4.0$ mm and $\rho = 0.45$ mm for both “MMG2F” and “MMC2D” models for $\sigma = 74$ MPa.

addition, the initial porosity is evaluated separately for each test. Indeed, a detailed study performed by [Lairinandrasana et al. \(2010\)](#) has demonstrated that the initial porosity measured experimentally of the undeformed PA6 varies between 1% and 2%. Although this discrepancy is quite acceptable from an experimental point of view, the numerical results are very sensitive to the initial porosity. The heterogeneous distribution of the initial porosity in the specimens is at the origin of a noticeable scatter of the long term creep behavior. Accordingly, initial damage is taken into account through $f_0 = f_0^a = f_0^c \neq 0$ for the models “MMG2F” et “MMG1F” and through $D_0 = D_0^a = D_0^c \neq 0$ for the models “MMC2D” et “MMC1D”. The different estimated values are displayed in [Table 5](#). The transition from secondary to tertiary creep corresponds to the minima of the strain rate. The optimized material parameters are listed in [Table 4](#) and the corresponding results are shown in [Figs. 4 and 5](#). It can be seen that the general trends are captured by the models and the δ values are also well reproduced. However, in terms of δ rate, the models underestimate the experimental values for the notch root radii ($\rho = 1.6$ and 0.8 mm). Note that δ is well predicted by the models for the notch root radii $\rho = 4$ and 0.45 mm except for the load level $\sigma = 78$ MPa. The triggering of the tertiary creep corresponding to damage initiation responsible of abrupt increase of strain is well simulated by the models “MMG2F” and “MMC2D”. In order to investigate the creep rate, the deformation of the notched specimen is defined as:

$$\varepsilon = \frac{\delta - \delta_{PL}}{\delta_0} \quad (44)$$

where δ_{PL} is the NOD corresponding to the end of the preloading stage and δ_0 is the initial NOD. The initial NODs corresponding to the different specimens are summarized in [Table 6](#). [Fig. 6](#) displays

the creep rate for the different notch radii and the load level for the models “MMC2D” and “MMG2F” only. In the light of these comparative results, it can be concluded that both MM models (coupled with GTN’s approach or with CDM theory) using a different damage variable per phase (i.e. “MMC2D” and “MMG2F”) correctly describe the primary, secondary and tertiary creep phenomena under high and low stress triaxiality ratio in opposition to the MM models with an overall damage variable for the PA6. Indeed, the model “MMC1D” underestimates the initiation time of the tertiary creep whereas the model “MMG1F” overestimates its start. In addition, both CDM theory and GTN’s approach are suitable for prediction of the behavior under low triaxiality ($\rho = 1.6$ and 4 mm) and high triaxiality ($\rho = 0.8$ and 0.45 mm). The proposed models are valid over a large time interval ranging from 0.4 h for the specimen with a notch radius $\rho = 4$ mm subjected to a creep stress of 78 MPa– 450 h for the specimen with $\rho = 0.45$ mm subjected to 70 MPa.

In terms of creep rates, models “MMC2D” and “MMG2F” are very close each other. [Fig. 6](#) shows the evolution of the creep rates of these two models together with the experimental results for the four notch radii ($\rho = 0.45, 0.8, 1.6$ and 4 mm) and the different applied creep stresses ($\sigma = 70, 74, 80$ MPa). Very good agreement between the experimental creep rates and the simulated ones can be depicted whatever the notch radius and whatever the applied creep stress in the primary, secondary and tertiary creep stages. The models “MMC2D” and “MMG2F” are then reliable for the creep life prediction of materials like PA6.

3.3. Analysis of numerical local results

From now on, models “MMC1D” and “MMG1F” will not be considered anymore because they fail to reproduce the overall

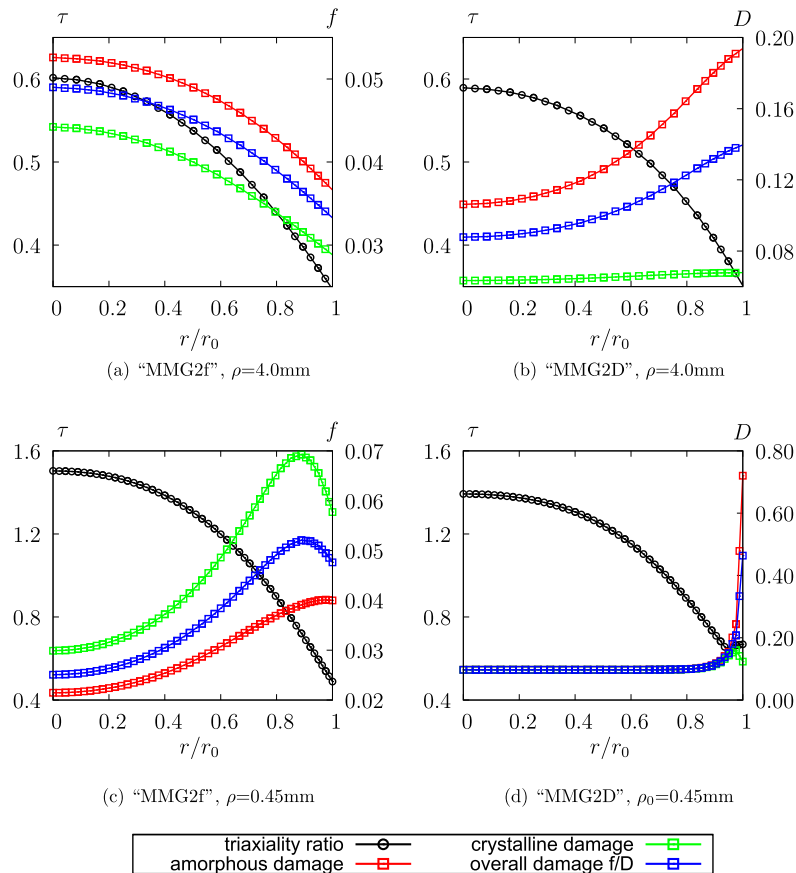


Fig. 10. Radial distribution of the damage variables corresponding to the minimal creep rate for $\sigma = 74$ MPa.

creep behavior of the notched specimens. The two retained models “MMC2D” and “MMG2f” are scrutinized in terms of local variables (triaxiality ratio τ , damages at the phase level and overall damage). In this paper, it will be shown that both models “MMC2D” and “MMG2f” accurately describe the experimental results. The model “MMG2f” will be selected for its pertinent prediction of the local informations such as damage. Qualitative comparison between experiments and the prediction of the model “MMG2f” is illustrated in Fig. 7. In that figure, the contour plot of the porosity predicted by the model “MMG2f” at the beginning of the tertiary creep stage (108,000 s for $\rho = 4$ mm, 504,000 s for $\rho = 0.45$ mm) is compared to whiteness of the experimental specimen. This is in conformity with the distribution of the porosity obtained in Sai et al. (2011). In this previous work, a thin horizontal intense whitening was observed in the net section for the smaller notch radius. However, light whitening was observed all along the stretched necking zone for the higher notch radius. The intensity of whitening indicates as was a substantial amount of damage. In the following, comparisons are performed for a creep stress of 74 MPa and two notch radii $\rho = 4.0$ mm and $\rho = 0.45$ mm corresponding to the lowest and the highest triaxiality ratio.

The amorphous damage (D_a or f_a), the crystalline damage (D_c or f_c), the overall damage (D or f) and the stress triaxiality ratio τ are plotted in Fig. 8 as function of the radial deformation $\Delta r/r_0$ following (Boisot et al., 2011) who investigated these variables in the center of minimal cross section. This kind of representation corresponds to a time distribution parameterized by $\Delta r/r_0$ and allows to distinguish more clearly the variation of the studied variables. The radial deformation usually linked to the volume change reaches a value of 14% for $\rho = 4.0$ mm and 4.5% for $\rho = 0.45$ mm. It

is observed that the triaxiality ratio τ exhibits the same profiles and levels for the two models “MMC2D” and “MMG2f” and for the two notch radii ($\rho = 4.0$ mm and $\rho = 0.45$ mm). The oscillations observed on τ are due to consecutive extension and re-necking during the notch root deformation (Boisot et al., 2011). Moreover, it can be noticed that the maximum damage moves during the loading along the axis of the specimen.

In the same Fig. 8 the simulated damage values are more pronounced for the model “MMC2D” compared with the model “MMG2f”.

The trace of the stress and strain tensors are also plotted in Fig. 9 as function of the radial deformation $\Delta r/r_0$. Very close results are obtained for the stress component with the two models “MMC2D” and “MMG2f”. The trace of the strain tensors (amorphous, crystalline and macroscopic) predicted using the GTN’s approach are slightly higher than those simulated by the CDM theory. It can be noted in particular that the strain tensor of the crystalline ($\text{Tr}(\boldsymbol{\varepsilon}^c)$) phase is quasi inactive at the beginning of the deformation stage. $\text{Tr}(\boldsymbol{\varepsilon}^c)$ increases rapidly and becomes predominant in comparison with $\text{Tr}(\boldsymbol{\varepsilon}^a)$ and $\text{Tr}(\boldsymbol{\varepsilon})$ for the model “MMG2f” in the case of $\rho = 0.45$. $\text{Tr}(\boldsymbol{\varepsilon}^c)$ also increases rapidly during the deformation but is attenuated at the end of the deformation stage for the model “MMC2D”.

The analysis of the local variables are performed along the radial direction of the net section in Figs. 10 and 11. The radial distribution of the variables τ , f , f^a , f^c , D , D^a and D^c corresponding to the minimal creep rate that lasts from the end of primary creep to the onset of tertiary creep for $\sigma = 74$ MPa is shown in Fig. 10 with both models “MMG2f” and “MMC2D” for the two notch radii ($\rho = 4.0$ mm and $\rho = 0.45$ mm). The times for which the creep rate

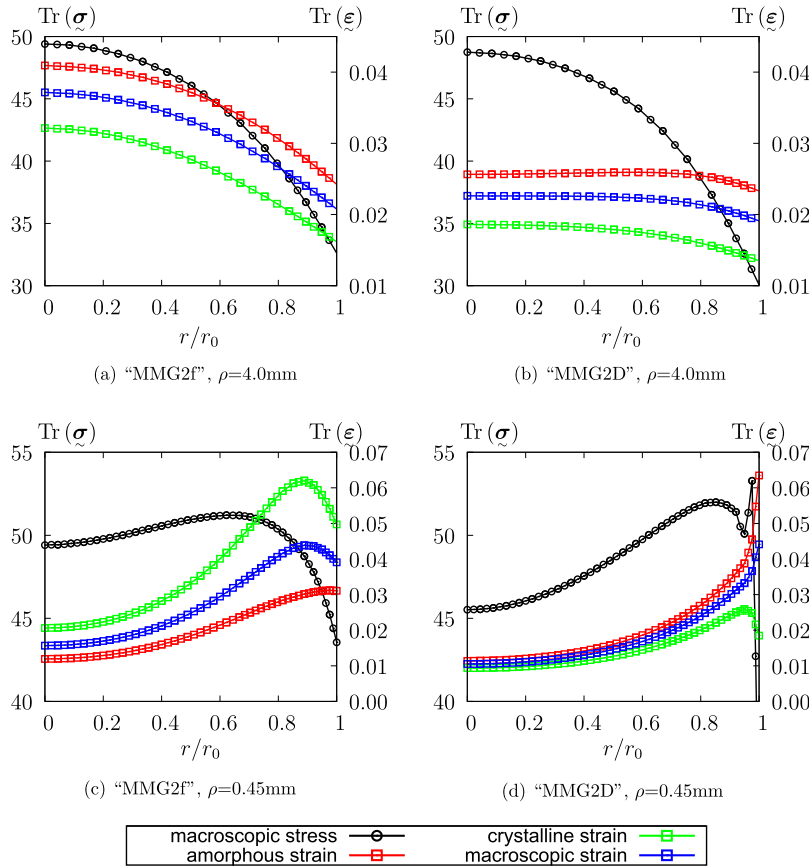


Fig. 11. Radial distribution stress and strain corresponding to the minimal creep rate for $\sigma = 74$ MPa.

Table 7

Time corresponding to the minimal creep rate for $\sigma = 74$ MPa.

Radius	"MMG2f"	"MMC2D"
$\rho = 4.0$ mm	96,011 s	96,977 s
$\rho = 0.45$ mm	398,938 s	496,511 s

is minimal are displayed in Table 7. A good adequacy is observed for the stress triaxiality ratio between the two models whatever the notch radius.

It is expected that the porosity follows the same trend as the triaxiality ratio. Surprisingly, Fig. 10c shows that is maximum in the center of the specimen whereas f reaches its maximum level in the vicinity of the notch root. This finding is in conformity with the results of Boisot et al. (2011) and can be explained by the fact that porosity is induced by $\text{Tr}(\tilde{\sigma})$ rather than the triaxiality ratio. In fact, by observing that the trend is similar for the porosity displayed in Fig. 10c and the $\text{Tr}(\sigma)$ shown in Fig. 11c, one can notice that this unexpected "τ" profile is essentially due to that of $J(\sigma)$. Moreover, this finding is in conformity with the results of Boisot et al. (2011) reporting that porosity is induced by $\text{Tr}(\sigma)$ rather than the stress triaxiality ratio. However, damage distributions for the two models completely differ. Indeed, for $\rho = 4.0$ mm, a decrease of the three damage variables (f, f^a and f^c) is depicted for the model "MMG2f". Whereas, D, D^a increase and D^c remains inactive. These opposite behaviors can also be noticed for $\rho = 0.45$ mm. For the model "MMG2f", the damage variables increase up to a maximal values located in the vicinity of the notch root and then decrease slightly. The damage variables predicted by the model "MMC2D" are very small and exhibit an abrupt increase to reach

high level at the center of the notch. The observation can also be confirmed according to the radial distribution of the stress and strain tensors shown in Fig. 11. The model "MMC2D" predicts a quasi constant strain tensors for $\rho = 4.0$ mm and identical amorphous, crystalline and overall behaviors.

The main concluding remarks may be summarized as follows.

- The volume change is mainly caused by the hydrostatic stress rather than the triaxiality ratio.
- The comparisons between simulations with the model "MMG2f" and experimental results show good accordance. The local contributions damage at each phase level are also correctly estimated thanks to the GTN's approach deduced from the micromechanical analysis.
- The "MMC2D" model is in good agreement with experimental behavior of the creep testing of notched specimens with both high notch radii (low triaxiality) and low notch radii (high triaxiality). Despite the fact that the "MMC2D" correctly reproduce the overall mechanical damage behavior, the analysis of the local variables such as the damage at the phase level reveals some shortcomings of the model that will need to be resolved. CDM theory accounts for defects through a homogenization concept and describes their growth macroscopically. Improvements can be brought by linking the damage evolution to the trace of the stress or the strain tensors.

4. Conclusion

This work aims at comparing two multi-mechanism models in simulating the mechanical damage behavior of semi crystalline polymers. The first model coupled with the GTN porous plasticity

approach whereas the second is based on the CDM theory. Two cases are considered for each model (i) damage is described by a unique overall variable (ii) each phase may be characterized by its own damage variable. The selection strategy consists of the following steps. First, the material parameters of the “undamaged material” common to all four models are identified by comparison to tensile and creep tests performed on smooth specimens. A first selection is then performed according to the predictive character of creep behavior of notched specimen with different notch radii. It is shown that models (GTN or CDM) with two damage variables describe better the macroscopic results. Finally, the local responses of the two remaining models are compared.

It can be concluded that MM model coupled with CDM theory using two damage variable is in good agreement with all experimental results. The MM model coupled with Gurson's approach and two damage variables describes correctly macroscopic experimental results, but also predicts pertinent local informations such as damage.

The damage considered in this paper consisted of initially spherical voids. However, it was shown for the PA6 material under study, that they are penny shaped with an evolving shape factor during deformation (Alexandre Cayzac, 2014; Laiarinandrasana et al., 2010). Moreover, these voids are generally stacked in columns, thus giving an arrangement in polar fans as reported by Pawlak and Galeski (2008), Pawlak and Galeski (2010), Rozanski and Galeski (2013). Ongoing work focuses on the experimental characterization of these voids in terms of their distributions in height and diameter within the net section. These distributions should then be utilized during the materials parameter calibration using inverse optimization method with the help of FE analysis. Another issue is to couple the optimization with unit cell computations that explicitly take void anisotropy into account.

References

- Abu Al-Rub, R., Tehrani, A., Darabi, M., 2014. Application of a large deformation nonlinear-viscoelastic viscoplastic viscodamage constitutive model to polymers and their composites. *Int. J. Damage Mech.*
- Ahzi, S., Makradi, A., Gregory, R., Edie, D., 2003. Modeling of deformation behavior and strain-induced crystallization in poly(ethylene terephthalate) above the glass transition temperature. *Mech. Mater.* 35, 1139–1148.
- Alexandre Cayzac, H., 2014. Analyses expérimentales et numérique de l'endommagement matriciel d'un matériau composite. Cas d'un pultrudé thermoplastique renforcé de fibres de verre (Ph.d. thesis). Ecole des Mines de Paris, in French.
- Andrade, F., de Sá, J.C., Pires, F., 2014. Assessment and comparison of non-local integral models for ductile damage. *Int. J. Damage Mech.* 23, 261–296.
- Ayoub, G., Naït-Abdelazi, M., Zairi, F., Gloaguen, J., Charrier, P., 2011. A continuum damage model for the high-cycle fatigue life prediction of styrene-butadiene rubber under multiaxial loading. *Int. J. Sol. Struct.* 48, 2458–2466.
- Baudet, C., Grandidier, J., Canémi, L., 2009. A two-phase model for the diffusomechanical behaviour of semicrystalline polymers in gaseous environment. *Int. J. Sol. Struct.* 46, 1389–1401.
- Bédoui, F., Diani, J., Régnier, G., 2004. Micromechanical modeling of elastic properties in polyolefins. *Polymer* 45, 2433–2442.
- BenHadj Hamouda, H., Laiarinandrasana, L., Piques, R., 2007. Viscoplastic behaviour of a medium density polyethylene (MDPE): constitutive equations based on double nonlinear deformation model. *Int. J. Plast.* 23, 1307–1327.
- Besson, J., Guillemer-Neel, C., 2003. An extension of the Green and Gurson models to kinematic hardening. *Mech. Mater.* 35, 1–18.
- Besson, J., Leriche, R., Foerch, R., Caillaud, G., 1998. Object-oriented programming applied to the finite element method. Part II. Application to material behaviors. *Rev. Eur. EF* 7, 567–588.
- Bles, G., Nowacki, W., Tourabi, A., 2009. Experimental study of the cyclic visco-elasto-plastic behaviour of a polyamide fibre strap. *Int. J. Sol. Struct.* 46, 2693–2705.
- Boisot, G., Laiarinandrasana, L., Besson, J., Fond, C., Hochstetter, G., 2011. Experimental investigations and modeling of volume change induced by void growth in polyamide 11. *Int. J. Sol. Struct.* 48, 2642–2654.
- Boudifa, M., Saanouni, K., Chaboche, J., 2009. A micromechanical model for inelastic ductile damage prediction in polycrystalline metals for metal forming. *Int. J. Mech. Sci.* 51, 453–464.
- Brunig, M., Gerke, S., Hagenbrock, V., 2013. Micro-mechanical studies on the effect of the stress triaxiality and the lode parameter on ductile damage. *Int. J. Plast.* 50, 49–65.
- Brusselle-Dupend, N., Cangémi, L., 2008. A two-phase model for the mechanical behaviour of semicrystalline polymers. Part II – modelling of the time-dependent mechanical behaviour of an isotropic and a highly oriented HDPE grade. *Mech. Mater.* 40, 761–770.
- Cayzac, H., Saï, K., Laiarinandrasana, L., 2013. Damage based constitutive relationships in semi-crystalline polymer by using multi-mechanisms model. *Int. J. Plast.* 51, 47–64.
- Chaboche, J., 1987. Continuum damage mechanics: present state and future trends. *Nucl. Eng. Des.* 105, 19–33.
- Chaboche, J., Boudifa, M., Saanouni, K., 2006. A CDM approach of ductile damage with plastic compressibility. *Int. J. Frac.* 137, 51–75.
- Colak, O., Krempel, E., 2005. Modeling of the monotonic and cyclic swift effects using an isotropic, finite viscoplasticity theory based on overstress (FVBO). *Int. J. Plast.* 21, 573–588.
- Cotterell, B., Chia, J., Hbaieb, K., 2007. Fracture mechanisms and fracture toughness in semicrystalline polymer nanocomposites. *Eng. Frac. Mech.* 74, 1054–1078.
- Danielsson, M., Parks, D., Boyce, M., 2002. Three-dimensional micromechanical modeling of voided polymeric materials. *J. Mech. Phys. Sol.* 50, 351–379.
- Detrez, F., Cantournet, S., Seguela, R., 2011. Plasticity/damage coupling in semicrystalline polymers prior to yielding: micromechanisms and damage law identification. *Polymer* 52, 1998–2008.
- Drozdo, A., 2010. Time-dependent response of polypropylene after strain reversal. *Int. J. Sol. Struct.* 47, 3221–3233.
- Drozdo, A., 2013. Mechanical response of polypropylene under multiple-step loading. *Int. J. Sol. Struct.* 50, 815–823.
- Drozdo, A., Christiansen, J., 2008. Thermo-viscoelastic and viscoplastic behavior of high-density polyethylene. *Int. J. Sol. Struct.* 45, 4274–4288.
- Dusunceli, N., Colak, O., 2007. Modelling the effects of degree of crystallinity on mechanical behavior of semicrystalline polymers. *Int. J. Plast.* 24, 1224–1242.
- Epee, A., Lauro, F., Bennani, B., Bourel, B., 2011. Constitutive model for a semicrystalline polymer under dynamic loading. *Int. J. Sol. Struct.* 48, 1590–1599.
- Faleskog, J., Gao, X., Shih, C., 1998. Cell model for nonlinear fracture analysis – I. Micromechanics calibration. *Int. J. Frac.* 89, 355–373.
- Frontini, P., Alejandra, L.F., Rueda, F., 2012. Non linear fracture mechanics of polymers: load separation and normalization methods. *Eng. Frac. Mech.* 79, 389–414.
- Gurson, A., 1977. Continuum theory of ductile rupture by void nucleation and growth. Part I: yield criteria and flow rules for porous ductile media. *J. Eng. Mat. Technol.* 99, 2–15.
- Hambli, R., 2001. Comparison between Lemaitre and Gurson damage models in crack growth simulation during blanking process. *Int. J. Mech. Sci.* 43, 2769–2790.
- Hambli, R., 2001. Finite element simulation of fine blanking processes using a pressure-dependent damage model. *J. Mat. Proc. Tech.* 116, 252–264.
- Ladeveze, P., 1999. *Nonlinear Computational Structural Mechanics – New Approaches and Non-Incremental Methods of Calculation*. Springer-Verlag.
- Laiarinandrasana, L., Morgener, T., Proudhon, H., Regrain, C., 2010. Damage of semicrystalline polyamide 6 assessed by 3D X-Ray tomography: from microstructural evolution to constitutive modeling. *J. Pol. Sci. B/Polym. Phys.* 48, 1516–1525.
- Leever, P., 2012. An engineering model for rapid crack propagation along fluid pressurized plastic pipe. *Eng. Frac. Mech.* 96, 539–557.
- Lemaitre, J., Desmorat, R., 2001. Section 6.14 – isotropic and anisotropic damage law of evolution. In: Lemaitre, J. (Ed.), *Handbook of Materials Behavior Models*. Academic Press, Burlington, pp. 513–524.
- Lemaitre, J., Desmorat, R., Sauzay, M., 2000. Anisotropic damage law of evolution. *Eur. J. Mech. A/Solids* 19, 187–208.
- Li, H., Fu, M., Lu, J., Yang, H., 2011. Ductile fracture: experiments and computations. *Int. J. Plast.* 27, 147–180.
- Malcher, L., Andrade Pires, F., César de Sá, J., 2012. An assessment of isotropic constitutive models for ductile fracture under high and low stress triaxiality. *Int. J. Plast.* 30–31, 81–115.
- Mkaddem, A., Hambli, R., Poirion, A., 2004. Comparison between Gurson and Lemaitre damage models in wiping die bending processes. *Int. J. Adv. Man. Tech.* 23, 451–461.
- Monchiet, V., Cazacu, O., Charkaluk, E., Kondo, D., 2008. Macroscopic yield criteria for plastic anisotropic materials containing spheroidal voids. *Int. J. Plast.* 24, 1158–1189.
- Nahshon, K., J.W. Hutchinson, J., 2008. Modification of the Gurson model for shear failure. *Int. J. Plast.* 27, 1–17.
- Nahshon, K., Xue, Z., 2009. A modified Gurson model and its application to punch-out experiments. *Eng. Frac. Mech.* 76, 997–1009.
- Nielsen, K., Tvergaard, V., 2009. Effect of a shear modified Gurson model on damage development in a FSW tensile specimen. *Int. J. Sol. Struct.* 46, 587–601.
- Nikolov, S., Doghri, I., 2000. A micro/macro constitutive model for the small deformation behavior of polyethylene. *Polymer* 41, 1883–1891.
- Ognedal, A., Clausen, A., Dahlen, A., Hopperstad, O., 2014. Behavior of PVC and HDPE under highly triaxial stress states: an experimental and numerical study. *Mech. Mater.* 72, 94–108.
- Oral, A., Anlas, G., Lambros, J., 2012. Determination of Gurson–Tvergaard–Needleman model parameters for failure of a polymeric material. *Int. J. Damage Mech.* 21, 3–25.
- Pardoen, T., Hutchinson, J., 2000. An extended model for void growth and coalescence. *J. Mech. Phys. Sol.* 48, 2467–2512.
- Pawlak, A., Galeski, A., 2008. Cavitation during tensile deformation of polypropylene. *Macromolecules* 41, 2839–2851.

- Pawlak, A., Galeski, A., 2010. Cavitation and morphological changes in polypropylene deformed at elevated temperatures. *J. Polym. Sci. Part B Polym. Phys.* 48, 1271–1280.
- Pirondi, A., Bonora, N., Steglich, D., Brocks, W., Hellmann, D., 2006. Simulation of failure under cyclic plastic loading by damage models. *Int. J. Plast.* 22, 2146–2170.
- Regrain, C., Laiarinandrasana, L., Toillon, S., 2009. Experimental and numerical study of creep and creep rupture behavior of PA6. *Eng. Frac. Mech.* 76, 2656–2665.
- Regrain, C., Laiarinandrasana, L., Toillon, S., Saï, K., 2009. Multi-mechanism models for semi-crystalline polymer: constitutive relations and finite element implementation. *Int. J. Plast.* 25, 1253–1279.
- Ricard, J., Guigné, F., Laiarinandrasana, L., 2014. Damage and fracture mechanisms of polyoxymethylene: multiscale experimental study and finite element modeling. *Eng. Frac. Mech.* 115, 270–283.
- Rozanski, A., Galeski, A., 2013. Plastic yielding of semicrystalline polymers affected by amorphous phase. *Int. J. Plast.* 41, 14–29.
- Saanouni, K., 2008. On the numerical prediction of the ductile fracture in metal forming. *Eng. Frac. Mech.* 75, 3545–3559.
- Saï, K., Laiarinandrasana, L., Ben Naceur, I., Besson, J., Jeridi, M., Cailletaud, G., 2011. Multi-mechanism damage-plasticity model for semi-crystalline polymer: creep damage of notched specimen of pa6. *Mater. Sci. Eng. A* 528, 1087–1093.
- Sheng, N., Boyce, M., Parks, D., Rutledge, G., Abes, J., Cohen, R., 2004. Multiscale micromechanical modeling of polymer/clay nanocomposites and the effective clay particle. *Polymer* 45, 487–506.
- Shojaei, A., Li, G., 2013. Viscoplasticity analysis of semicrystalline polymers: a multiscale approach within micromechanics framework. *Int. J. Plast.* 42, 31–49.
- Stoer, J., 1985. Principles of sequential quadratic programming methods for solving nonlinear programs. In: Schittkowski, K. (Ed.), *NATO ASI Series*, vol. 15. Springer Verlag, Berlin.
- Tvergaard, V., Nielsen, K., 2010. Relations between a micro-mechanical model and a damage model for ductile failure in shear. *J. Mech. Phys. Sol.* 58, 1243–1252.
- van Dommelen, J., Parks, D., Boyce, M., Brekelmans, W., Baaijens, F., 2003. Micromechanical modeling of the elasto-viscoplastic behavior of semicrystalline polymers. *J. Mech. Phys. Sol.* 51, 519–541.
- Wang, L., Zhou, F., Sun, Z., Wang, Y., Shi, S., 2010. Studies on rate-dependent macro-damage evolution of materials at high strain rates. *Int. J. Damage Mech.* 19, 805–820.
- Zaïri, F., Naït-Abdelaziz, M., Gloaguen, J., Lefebvre, J., 2011. A physically-based constitutive model for anisotropic damage in rubber-toughened glassy polymers during finite deformation. *Int. J. Plast.* 27, 25–51.